

ARTICLE IN PRESS



ELSEVIER

Available online at www.sciencedirect.com

ScienceDirect

Comput. Methods Appl. Mech. Engrg. xxx (xxxx) xxx

**Computer methods
in applied
mechanics and
engineering**www.elsevier.com/locate/cma

Highlights

A scalable exponential-DG approach for nonlinear conservation laws: With application to Burger and Euler equations

Shinhoo Kang*, Tan Bui-Thanh

Comput. Methods Appl. Mech. Engrg. xxx (xxxx) xxx

- Exponential-DG is stable with a large Courant number; and high-order in time/space.
- Exponential-DG outperforms over IMEX-DG methods with no preconditioner.
- Exponential-DG is comparable to RK-DG for stiff problems.
- Exponential-DG is scalable in a modern massively parallel computing architecture.
- Present stability and convergence analyses for the exponential Euler DG scheme.

Graphical abstract and Research highlights will be displayed in online search result lists, the online contents list and the online article, but **will not appear in the article PDF file or print unless it is mentioned in the journal specific style requirement. They are displayed in the proof pdf for review purpose only.**



ELSEVIER

Available online at www.sciencedirect.com

ScienceDirect

Comput. Methods Appl. Mech. Engrg. xxx (xxxx) xxx

**Computer methods
in applied
mechanics and
engineering**

www.elsevier.com/locate/cma

A scalable exponential-DG approach for nonlinear conservation laws: With application to Burger and Euler equations

Shinhoo Kang^{a,*}, Tan Bui-Thanh^b

^a *Mathematics and Computer Science Division Argonne National Laboratory Lemont, IL 60439, USA*

^b *Department of Aerospace Engineering and Engineering Mechanics, and Oden Institute for Computational Engineering & Sciences, The University of Texas at Austin, Austin, TX 78712, USA*

Received 2 November 2020; received in revised form 16 April 2021; accepted 1 July 2021

Available online xxx

Abstract

We propose an Exponential DG approach for numerically solving partial differential equations (PDEs). The idea is to decompose the governing PDE operators into linear (fast dynamics extracted by linearization) and nonlinear (the remaining after removing the former) parts, on which we apply the discontinuous Galerkin (DG) spatial discretization. The resulting semi-discrete system is then integrated using exponential time-integrators: exact for the former and approximate for the latter. By construction, our approach i) is stable with a large Courant number ($Cr > 1$); ii) supports high-order solutions both in time and space; iii) is computationally favorable compared to IMEX DG methods with no preconditioner; iv) requires comparable computational time compared to explicit RKDG methods, while having time stepsizes orders magnitude larger than maximal stable time stepsizes for explicit RKDG methods; v) is scalable in a modern massively parallel computing architecture by exploiting Krylov-subspace matrix-free exponential time integrators and compact communication stencil of DG methods. Various numerical results for both Burgers and Euler equations are presented to showcase these expected properties. For Burgers equation, we present a detailed stability and convergence analyses for the exponential Euler DG scheme.

© 2021 Elsevier B.V. All rights reserved.

Keywords: Exponential integrators; Discontinuous Galerkin methods; Euler systems; Burgers equation

1. Introduction

The discontinuous Galerkin (DG) method has gain popularity for decades as a spatial discretization. The DG method—originally developed [1–3] for the neutron transport equation—has been studied extensively for various types of partial differential equations (PDEs) including Poisson type equation [4–7], poroelasticity [8], shallow water equations [9–12], Euler and Navier–Stokes equations [13,14], Maxwell equations [15,16], solid dynamics [17], magma dynamics [18], to name a few. One of the reason is that DG methods are well-suited for parallel-computing due to the local nature of the methods. DG methods combine advantages of finite volume and finite element methods in the sense that a global solution is approximated by a finite set of local functions, and each local element communicates with its adjacent element through numerical flux on element boundary. Since the numerical

* Corresponding author.

E-mail addresses: shinhoo.kang@anl.gov (S. Kang), tanbui@oden.utexas.edu (T. Bui-Thanh).

flux is calculated using the state variables on the face, DG methods have compact stencil, hence reduces inter-communication cost. Another reason can be the positive properties of the scheme, i.e., flexibility for handling complex geometry, hp-adaptivity, high-order accuracy, upwind stabilization, etc. [4–7,19].

To fully discretize a time-dependent partial differential equation (PDE), temporal discretization is also necessary. Explicit time integrators such as Runge–Kutta methods are popular due to their simplicity and ease in computer implementation. However, scale-separated or geometrically-induced stiffness limits the time-step size severely for high-order DG methods (see, e.g., [20,10]). For long-time integration this can lead to an excessive number of time steps, and hence substantially taxing computing and storage resources. On the other hand, fully-implicit methods could be expensive, especially for nonlinear PDEs for which Newton-like methods are typically required. Semi-implicit time-integrators have been designed to relax the time-step size restriction caused by the stiffness in order to reduce the computational burden arising from the linear solve [21–23]. In the context of low-speed fluid flows, including Euler, Navier–Stokes, and shallow water equations, implicit–explicit (IMEX) DG methods have been proposed and demonstrated to be more advantageous than either explicit or fully-implicit DG methods [24–26]. The common feature of these methods is that they relax the stiffness condition by employing implicit time-stepping schemes for handling the linear stiff part of the PDE. Therefore the performance highly depends on a linear solver, which means an appropriate preconditioner needs to be constructed for achieving decent performance. However, developing such a preconditioner is not a trivial task and it is problem-specific.

Alternatively, exponential time integrators have been received great attention due to the positive characteristics such as stability and accuracy. The methods have been applied to various types of PDEs including linear advection–diffusion equations [27], Schrödinger equation [28], Maxwell equations [29], magnetohydrodynamics (MHD) equations [30], Euler equations [31], incompressible Navier–Stokes equations [32], compressible Navier–Stokes equations [33,34], shallow water equations [35], among others.

Exponential time integrators are similar to IMEX methods in the sense of splitting a governing equation into stiff and non-stiff parts. However, exponential time integrators exactly integrate the linear stiff part by multiplying an integrating factor instead of using a quadrature in time. Compared to IMEX methods, exponential time integrators replace a linear solve at each time step with a computationally demanding matrix exponential.

Many researchers have conducted various studies to mitigate the challenge, one way is to use Krylov subspace, where a large matrix is projected onto a small Krylov subspace so that computing the matrix exponential becomes less expensive. To improve the Krylov subspace projection-based algorithm, rational Krylov method [36,37], restart Krylov method [38,39], block Krylov method [40,41], adaptive Krylov method [42] have been developed. Lately, [43] and [44] enhance the computational efficiency of the adaptive Krylov method by replacing the Arnoldi procedure [45] with the incomplete orthogonalization procedure [46,47]. The work in [48] shows that the exponential propagation iterative (EPI) schemes can outperform the standard implicit Newton–Krylov integrators with no preconditioning. The work in [35] observes the second-order EPI2 provides comparable results to the explicit fourth-order Runge–Kutta (RK4). For elastodynamic problems, the second-order Gautschi-type exponential integrator outperforms the backward Euler integrators [49,50].

In this study, we propose an Exponential DG framework for partial differential equations. To that end, we separate governing equations into linear and nonlinear parts, to which we apply the DG spatial discretization. The former is integrated analytically, whereas the latter is approximated. Since the method does not require any linear solve, it has a potential to be scalable in a modern massively parallel computing architecture. The proposed Exponential DG method: (i) is stable with a large Courant number ($Cr > 1$); (ii) exploits high-order solutions both in time and space; (iii) is more efficient than IMEX DG methods with no preconditioner; (iv) is comparable to explicit RKDG methods on uniform mesh and more beneficial on non-uniform grid for Euler equations; (v) provides promising weak and strong scalable parallel solutions.

In the following, we discuss Exponential DG framework in Section 2. In Section 3, we apply Exponential DG framework to Burgers equation and Euler equations, where we show the construction of linear operator based on a flux Jacobian. Then, we present a detailed analysis on the stability and convergence of the exponential DG scheme for Burgers equation. The performance of the proposed method will be discussed in Section 5 with several numerical examples for both Burgers and Euler equations. We finally conclude the paper in Section 6.

2. Exponential DG framework

In this section, we present the key idea behind Exponential DG framework. We first split a given PDE into a linear and a nonlinear parts, to which DG discretization and exponential time integrators are applied. We begin with notations and conventions used in the paper.

2.1. Finite element definitions and notations

Let Ω be an open and bounded subset of \mathbb{R}^d , where $d = \{1, 2, 3\}$ is the spatial dimension. We denote by $\Omega_h := \cup_{i=1}^{N_{el}} K_i$ the mesh containing a finite collection of non-overlapping elements, K_i , that partition Ω . Here, h is defined as $h := \max_{j \in \{1, \dots, N_{el}\}} \text{diam}(K_j)$. Let $\partial\Omega_h := \{\partial K : K \in \Omega_h\}$ be the collection of the faces of all elements. Let us define \mathcal{E}_h as the skeleton of the mesh which consists of the set of all uniquely defined faces. For two neighboring elements K^+ and K^- that share an interior interface $e = K^+ \cap K^-$, we denote by q^\pm the trace of their solutions on e . We define \mathbf{n}^- as the unit outward normal vector on the boundary ∂K^- of element K^- , and $\mathbf{n}^+ = -\mathbf{n}^-$ the unit outward normal of a neighboring element K^+ . On the interior interfaces $e \in \mathcal{E}_h^o$, we define the mean/average operator $\{\mathbf{v}\}$, where \mathbf{v} is either a scalar or a vector quantity, as $\{\mathbf{v}\} := (\mathbf{v}^- + \mathbf{v}^+)/2$, and the jump operator $[\mathbf{v}] := 2\{\mathbf{v} \cdot \mathbf{n}\}$. On the boundary faces $e \in \mathcal{E}_h^b$, unless otherwise stated, we define the mean and jump operators as $\{\mathbf{v}\} := \mathbf{v}$, $[\mathbf{v}] := \mathbf{v} \cdot \mathbf{n}$.

Let $\mathcal{P}^k(D)$ denote the space of polynomials of degree at most k on a domain D . Next, we introduce discontinuous piecewise polynomial spaces for scalars and vectors as

$$\begin{aligned} V_h(\Omega_h) &:= \{v \in L^2(\Omega_h) : v|_K \in \mathcal{P}^k(K), \forall K \in \Omega_h\}, \\ \Lambda_h(\mathcal{E}_h) &:= \{\lambda \in L^2(\mathcal{E}_h) : \lambda|_e \in \mathcal{P}^k(e), \forall e \in \mathcal{E}_h\}, \\ \mathbf{V}_h(\Omega_h) &:= \{\mathbf{v} \in [L^2(\Omega_h)]^m : \mathbf{v}|_K \in [\mathcal{P}^k(K)]^m, \forall K \in \Omega_h\}, \\ \mathbf{\Lambda}_h(\mathcal{E}_h) &:= \{\boldsymbol{\lambda} \in [L^2(\mathcal{E}_h)]^m : \boldsymbol{\lambda}|_e \in [\mathcal{P}^k(e)]^m, \forall e \in \mathcal{E}_h\}. \end{aligned}$$

and similar spaces $V_h(K)$, $\Lambda_h(e)$, $\mathbf{V}_h(K)$, and $\mathbf{\Lambda}_h(e)$ by replacing Ω_h with K and \mathcal{E}_h with e . Here, m is the number of components of the vector under consideration.

We define $\langle \cdot, \cdot \rangle_K$ as the L^2 -inner product on an element $K \in \mathbb{R}^d$, and $\langle \cdot, \cdot \rangle_{\partial K}$ as the L^2 -inner product on the element boundary $\partial K \in \mathbb{R}^{d-1}$. We also define the broken inner products as $\langle \cdot, \cdot \rangle_\Omega := \langle \cdot, \cdot \rangle_{\Omega_h} := \sum_{K \in \Omega_h} \langle \cdot, \cdot \rangle_K$ and $\langle \cdot, \cdot \rangle_{\partial\Omega} := \langle \cdot, \cdot \rangle_{\partial\Omega_h} := \sum_{\partial K \in \partial\Omega_h} \langle \cdot, \cdot \rangle_{\partial K}$, and on the mesh skeleton as $\langle \cdot, \cdot \rangle_{\mathcal{E}_h} := \sum_{e \in \mathcal{E}_h} \langle \cdot, \cdot \rangle_e$. We also define associated norms as $\|\cdot\|_{\Omega_h} := \left(\sum_{K \in \Omega_h} \|\cdot\|_K^2\right)^{\frac{1}{2}}$ and $\|\cdot\|_{\partial\Omega_h} := \left(\sum_{\partial K \in \partial\Omega_h} \|\cdot\|_{\partial K}^2\right)^{\frac{1}{2}}$ where $\|\cdot\|_K = \langle \cdot, \cdot \rangle_K^{\frac{1}{2}}$ and $\|\cdot\|_{\partial K} = \langle \cdot, \cdot \rangle_{\partial K}^{\frac{1}{2}}$.

2.2. Constructing linear and nonlinear DG operators for conservation laws

We consider conservation laws governed by a generic system of partial differential equation (PDE):

$$\frac{\partial \mathbf{q}}{\partial t} + \nabla \cdot \mathcal{F} = \mathbf{s}, \quad \text{in } \Omega, \quad (1)$$

where \mathbf{q} is the conservative variable, $\mathcal{F} = \mathcal{F}(\mathbf{q})$ is the flux tensor, and \mathbf{s} is the source vector. We seek a stiff linear flux \mathcal{F}_L that, we assume, captures the rapidly changing dynamics in the system. Inspired by the works in [48,51], we use a flux Jacobian to define the linear flux, i.e.,

$$\mathcal{F}_L := \frac{\partial \mathcal{F}}{\partial \mathbf{q}} \Big|_{\tilde{\mathbf{q}}} \mathbf{q}, \quad (2)$$

where $\tilde{\mathbf{q}}$ is a reference state. By adding and subtracting the linear flux \mathcal{F}_L in (1), we split the divergence term into a linear (stiff) part $\nabla \cdot \mathcal{F}_L$ and a nonlinear (non-stiff) part $\nabla \cdot (\mathcal{F} - \mathcal{F}_L)$. Similarly, we decompose the source term \mathbf{s} into a linear term \mathbf{s}_L ,

$$\mathbf{s}_L := \frac{\partial \mathbf{s}}{\partial \mathbf{q}} \Big|_{\tilde{\mathbf{q}}} \mathbf{q}, \quad (3)$$

and a nonlinear term $\mathbf{s} - \mathbf{s}_L$. Thus (1) becomes

$$\frac{\partial \mathbf{q}}{\partial t} + \nabla \cdot \mathcal{F}_L + \nabla \cdot \mathcal{F}_N = \mathbf{s}_L + \mathbf{s}_N \quad (4)$$

at the continuous level, where $\mathcal{F}_N = \mathcal{F} - \mathcal{F}_L$ and $\mathbf{s}_N = \mathbf{s} - \mathbf{s}_L$. The decomposition at continuous level avoids complicated derivatives of the stabilization parameter coming from a numerical flux in DG methods when applying

exponential time integrators. To the rest of the paper, except for the analysis in Section 4, we use the same notations for the exact and the DG solutions for simplicity. A semi-discrete form of (4) using DG discretization for spatial derivatives reads: find $\mathbf{q} \in \mathbf{V}_h(\Omega_h)$ such that

$$\left(\frac{\partial \mathbf{q}}{\partial t}, \mathbf{v} \right)_{\Omega_h} = \langle L\mathbf{q}, \mathbf{v} \rangle + \langle \mathcal{N}(\mathbf{q}), \mathbf{v} \rangle, \quad (5)$$

for all $\mathbf{v} \in \mathbf{V}_h(\Omega_h)$, where

$$\begin{aligned} \langle \mathcal{N}(\mathbf{q}), \mathbf{v} \rangle &:= -(\nabla \cdot \mathcal{F}_{\mathcal{N}}(\mathbf{q}), \mathbf{v})_{\Omega_h} + (\mathbf{s}_{\mathcal{N}}(\mathbf{q}), \mathbf{v})_{\Omega_h} - \langle (\mathcal{F}_{\mathcal{N}}^*(\mathbf{q}^\pm) - \mathcal{F}_{\mathcal{N}}(\mathbf{q})) \cdot \mathbf{n}, \mathbf{v} \rangle_{\partial\Omega_h}, \\ \langle L\mathbf{q}, \mathbf{v} \rangle &:= -(\nabla \cdot \mathcal{F}_L(\mathbf{q}), \mathbf{v})_{\Omega_h} + (\mathbf{s}_L(\mathbf{q}), \mathbf{v})_{\Omega_h} - \langle (\mathcal{F}_L^*(\mathbf{q}^\pm) - \mathcal{F}_L(\mathbf{q})) \cdot \mathbf{n}, \mathbf{v} \rangle_{\partial\Omega_h}. \end{aligned}$$

Here, \mathcal{F}_L^* and $\mathcal{F}_{\mathcal{N}}^* := \mathcal{F}^* - \mathcal{F}_L^*$ are a linear and a nonlinear DG numerical flux, respectively, such that

$$\langle [\mathcal{F}_{\mathcal{N}}^*(\mathbf{q}^\pm) \cdot \mathbf{n}], \hat{\mathbf{v}} \rangle_{\mathcal{E}_h} = 0 \text{ and } \langle [\mathcal{F}_L^*(\mathbf{q}^\pm) \cdot \mathbf{n}], \hat{\mathbf{v}} \rangle_{\mathcal{E}_h} = 0, \quad (6)$$

for all $\hat{\mathbf{v}} \in A_h(\mathcal{E}_h)$. At this point both spatial linear and the nonlinear operators are discretized with DG, and we discuss exponential time integrators for temporal derivative next.

2.3. Exponential time integrators

For the clarity of the exposition, let us rewrite (5) as

$$\frac{d\mathbf{q}}{dt} = L\mathbf{q} + \mathcal{N}(\mathbf{q}), \quad t \in (0, T), \quad (7)$$

with an initial condition $\mathbf{q}_0 = \mathbf{q}(0)$. An abuse of notations has been made for brevity: first, the proper form for both L and \mathcal{N} would be a composition with a projection operator onto $V_h(\Omega_h)$ as in Section 4; second, we do not distinguish \mathbf{q} with its nodal (or modal) vector; and third, L and \mathcal{N} are used interchangeably with their matrix representations from $V_h(\Omega_h)$ to $V_h(\Omega_h)$ (see also Section 4). Now multiplying (6) with integrating factor $e^{-\Delta t L}$ yields

$$\mathbf{q}(t^{n+1}) = e^{\Delta t L} \mathbf{q}(t^n) + \int_0^{\Delta t} e^{(\Delta t - \sigma)L} \mathcal{N}(\mathbf{q}(t^n + \sigma)) d\sigma \quad (8)$$

via a simple application of the method of variation of constants. At this point, (7) is exact. The first term $e^{\Delta t L} \mathbf{q}(t^n)$ is the homogeneous solution, whereas the second term is the particular solution that involves a convolution integral with the matrix exponential. Various exponential integrators have been proposed to approximate (7) in different ways. In particular, a p th-order time polynomial approximation to the nonlinear map \mathcal{N} can be written as

$$\mathcal{N}(\mathbf{q}(t^n + \sigma)) = \sum_{j=0}^{p-1} \frac{(t^n + \sigma)^j}{j!} \mathbf{v}_{j+1} + \mathcal{O}(\Delta t^p), \quad (9)$$

with appropriate choice [52] for \mathbf{v}_j . This allows us to express an approximation of $\mathbf{q}(t^{n+1})$ in (7), denoted as \mathbf{q}^{n+1} , as a linear combination of φ -functions [42], i.e.,

$$\mathbf{q}^{n+1} = \sum_{i=0}^p (\Delta t)^i \varphi_i(\Delta t L) \mathbf{b}_i, \quad (10)$$

where we have defined $\mathbf{b}_0 := \mathbf{q}(t^n)$ and $\mathbf{b}_i := \sum_{j=0}^{p-i} \frac{(t^n)^j}{j!} \mathbf{v}_{i+j}$. Here, φ_i -functions for a scalar τ are defined by

$$\varphi_i(\tau) := \int_0^1 e^{(1-z)\tau} \frac{z^{i-1}}{(i-1)!} dz \quad (11)$$

with $\varphi_0(\tau) := e^\tau$. It is easy to see the recurrence relation $[\varphi_i(\tau) - \varphi_i(0)] \tau^{-1} = \varphi_{i+1}(\tau)$ and $\varphi_i(0) = \frac{1}{i!}$ hold true. The definition of φ_i -functions for matrices is straightforward, e.g., based on Jordan canonical form [53].

For efficient computation of (8), Krylov subspace methods [54–56] with the exponential of the augmented matrix can be used [57,58,42,43], in which an augmented matrix is constructed and projected onto a small Krylov subspace so that matrix exponential is amenable to compute.

1 In this paper, we use KIOPS [43] algorithm¹ for serial computations. For parallel computation, we have
 2 implemented an exponential time integrator based on the KIOPS algorithm for our C++ DG finite element library
 3 (a spin-off from mangl1 [59]). Thanks to DG discretization and explicit nature of the exponential integrators, the
 4 proposed method is highly parallel as the communication cost can be effectively overlapped by computation.

5 3. Model problems

6 The key in the operator splitting in (5) is the linearized flux \mathcal{F}_L (2). In this section we choose Burgers and Euler
 7 equations as prototypes for the generic conservation law (1) and construct \mathcal{F}_L (hence L and \mathcal{N}) for these equations.

8 3.1. Burgers equation

9 Burgers equation is a quasi-linear parabolic PDE that comprises of nonlinear convection and linear diffusion:

$$10 \quad \frac{\partial u}{\partial t} + \frac{1}{2} \frac{\partial u^2}{\partial x} = \frac{\partial}{\partial x} \left(\kappa \frac{\partial u}{\partial x} \right) \text{ in } \Omega, \quad (9)$$

11 where u is a scalar quantity and $\kappa > 0$ is the constant viscosity. The linearization \mathcal{F}_L (2) of $\mathcal{F} := u^2/2 - \kappa \frac{\partial u}{\partial x}$
 12 evaluated at \tilde{u} is given by

$$13 \quad \mathcal{F}_L := \tilde{u}u - \kappa \frac{\partial u}{\partial x},$$

14 and thus

$$15 \quad \mathcal{F}_N := \frac{u^2}{2} - \tilde{u}u.$$

16 We can now write (9) in the form (4) as

$$17 \quad \frac{\partial u}{\partial t} + \frac{\partial}{\partial x} \underbrace{\left(\tilde{u}u - \kappa \frac{\partial u}{\partial x} \right)}_{\mathcal{F}_L} + \frac{\partial}{\partial x} \underbrace{\left(\frac{u^2}{2} - \tilde{u}u \right)}_{\mathcal{F}_N} = 0 \text{ in } \Omega \quad (10)$$

where \tilde{u} is a reference state (for example $\tilde{u} = u^n$: the numerical solution at t^n). The DG weak formulation of (10)
 reads: seek $q, u \in V_h(\Omega_h)$ such that

$$(q, p)_{\Omega_h} = \left(\frac{\partial u}{\partial x}, p \right)_{\Omega_h} + \langle \mathbf{n}(u^{**} - u), p \rangle_{\partial\Omega_h}, \quad (11a)$$

$$\left(\frac{\partial u}{\partial t}, v \right)_{\Omega_h} := \langle Lu, v \rangle + \langle \mathcal{N}(u), v \rangle, \quad (11b)$$

where

$$\langle Lu, v \rangle := - \left(\kappa q - \tilde{u}u, \frac{\partial v}{\partial x} \right)_{\Omega_h} + \langle \mathbf{n}(\kappa q^{**} - (\tilde{u}u)^*), v \rangle_{\partial\Omega_h}, \quad (12a)$$

$$\langle \mathcal{N}(u), v \rangle := - \left(\tilde{u}u - \frac{1}{2}u^2, \frac{\partial v}{\partial x} \right)_{\Omega_h} + \left\langle \mathbf{n} \left((\tilde{u}u)^* - \left(\frac{u^2}{2} \right)^* \right), v \right\rangle_{\partial\Omega_h}, \quad (12b)$$

18 for all $p, v \in V_h(\Omega_h)$ with $\mathbf{n} = \pm 1$ for one-dimensional problems. Here, we use the central flux for u^{**} and
 19 q^{**} for diffusion operator, i.e., $q^{**} = \{q\}$ and $u^{**} = \{u\}$, the entropy flux for inviscid Burgers part, i.e., $\left(\frac{u^2}{2}\right)^* :=$
 20 $\frac{1}{3} \left(\left\{ \frac{1}{2}u^2 \right\} + \{u\}^2 \right) + \frac{\sigma}{h} [u]$, where $\sigma \geq 0$ is a constant (the Lax–Friedrichs flux $\left(\frac{u^2}{2}\right)^* := \left\{ \frac{1}{2}u^2 \right\} + \frac{1}{2} \max(|u^\pm|) [u]$ is
 21 also considered to compare with the entropy flux), and the Lax–Friedrichs flux for linear Jacobian part, i.e., $(\tilde{u}u)^* :=$
 22 $\{\tilde{u}u\} + \frac{1}{2} \max(|\tilde{u}^\pm|) [u]$. With the central flux u^{**} , q can be computed locally element-by-element from (11a), and
 23 the only actual (global) unknown is u in (11).

¹ The performance of the adaptive Krylov subspace solver depends on several parameters such as the size of Krylov space. We empirically determine the parameters in this studies.

3.2. Euler equations

1

We consider the compressible Euler equations written in the following form

$$\frac{\partial \rho}{\partial t} + \nabla \cdot (\rho \mathbf{u}) = 0, \quad (13a)$$

$$\frac{\partial \rho \mathbf{u}}{\partial t} + \nabla \cdot (\rho \mathbf{u} \otimes \mathbf{u} + p \mathcal{I}) = 0, \quad (13b)$$

$$\frac{\partial \rho E}{\partial t} + \nabla \cdot (\rho \mathbf{u} H) = 0, \quad (13c)$$

where ρ is the density, \mathbf{u} the velocity, p the pressure, $\rho E = \rho e + \frac{1}{2} \rho \|\mathbf{u}\|^2$ the total energy, $e = \frac{p}{\rho(\gamma-1)}$ the internal energy, p the pressure, $H = E + \frac{p}{\rho} = \frac{a^2}{\gamma-1} + \frac{1}{2} \|\mathbf{u}\|^2$ the total specific enthalpy, $a = \sqrt{\gamma p / \rho}$ the sound speed, γ the ratio of the specific heat, and \mathcal{I} the $d \times d$ identity matrix. In a compact form, (13) can be written as

$$\frac{\partial \mathbf{q}}{\partial t} + \nabla \cdot \mathcal{F}(\mathbf{q}) = 0, \quad (14)$$

with $\mathbf{q} = (\rho, \rho \mathbf{u}, \rho E)^T$, $\mathbf{s} = (s_\rho, s_{\rho \mathbf{u}}, s_{\rho E})^T$, and $\mathcal{F}(\mathbf{q}) = (\rho \mathbf{u}, \rho \mathbf{u} \otimes \mathbf{u} + p \mathcal{I}, \rho \mathbf{u} H)^T$. Let us define $u_\nu := \mathbf{n} \cdot \mathbf{u}$, $\phi := \left(\frac{\gamma-1}{2}\right) \|\mathbf{u}\|^2$, $\tilde{\gamma} := \gamma - 1$, the flux Jacobian $A := \frac{\partial \mathcal{F}}{\partial \mathbf{q}}$ where

$$A = \begin{pmatrix} 0 & \mathbf{n}^T & 0 \\ \phi \mathbf{n} - \mathbf{u} u_\nu & \mathbf{u} \otimes \mathbf{n} - \tilde{\gamma} \mathbf{n} \otimes \mathbf{u} + u_\nu \mathcal{I} & \tilde{\gamma} \mathbf{n} \\ (\phi - H) u_\nu & H \mathbf{n}^T - \tilde{\gamma} \mathbf{u}^T u_\nu & \gamma u_\nu \end{pmatrix}. \quad (8)$$

The linearized flux (2) in this case is defined $\mathcal{F}_L := A(\tilde{\mathbf{q}})\mathbf{q} =: \tilde{A}\mathbf{q}$, and (4) now reads

$$\frac{\partial \mathbf{q}}{\partial t} + \nabla \cdot \underbrace{(\tilde{A}\mathbf{q})}_{\mathcal{F}_L} + \nabla \cdot \underbrace{(\mathcal{F}(\mathbf{q}) - \tilde{A}\mathbf{q})}_{\mathcal{F}_N} = \mathbf{0}. \quad (15)$$

By multiplying a test function \mathbf{v} to (15), integrating by parts for each element, and summing all the elements we arrive at the semi-discretization with DG: seek $\mathbf{q} \in \mathbf{V}_h(\Omega_h)$ such that

$$\left(\frac{\partial \mathbf{q}}{\partial t}, \mathbf{v} \right)_{\Omega_h} = \langle L\mathbf{q}, \mathbf{v} \rangle + \langle \mathcal{N}(\mathbf{q}), \mathbf{v} \rangle, \quad \forall \mathbf{v} \in \mathbf{V}_h(\Omega_h), \quad (13)$$

where

$$\begin{aligned} \langle L\mathbf{q}, \mathbf{v} \rangle &:= \left(\tilde{A}\mathbf{q}, \nabla \mathbf{v} \right)_{\Omega_h} - \left\langle \left(\tilde{A}\mathbf{q} \right)^* \cdot \mathbf{n}, \mathbf{v} \right\rangle_{\partial \Omega_h}, \\ \langle \mathcal{N}(\mathbf{q}), \mathbf{v} \rangle &:= - \left(\tilde{A}\mathbf{q} - \mathcal{F}(\mathbf{q}), \nabla \mathbf{v} \right)_{\Omega_h} + \left\langle \left(\left(\tilde{A}\mathbf{q} \right)^* - \mathcal{F}^*(\mathbf{q}) \right) \cdot \mathbf{n}, \mathbf{v} \right\rangle_{\partial \Omega_h}. \end{aligned}$$

For this work, we use the Roe flux [60] for both linear and nonlinear fluxes, i.e.,

$$\begin{aligned} \mathcal{F}^*(\mathbf{q}^\pm) &= \{\mathcal{F}(\mathbf{q})\} + \frac{1}{2} |A(\mathbf{q}_{Roe}^*)| [\mathbf{n} \cdot \mathbf{q}], \\ \left(\tilde{A}\mathbf{q}^\pm \right)^* &= \left\{ \left\{ \tilde{A}\mathbf{q} \right\} \right\} + \frac{1}{2} |A(\tilde{\mathbf{q}}_{Roe}^*)| [\mathbf{n} \cdot \mathbf{q}], \end{aligned}$$

where \mathbf{q}_{Roe}^* and $\tilde{\mathbf{q}}_{Roe}^*$ are Roe average states,² and $|A| := R|\Lambda|R^{-1}$ with (Λ, R) as the eigen-pairs of A (see, e.g [61], 14 for more details). 15

3.2.1. Artificial viscosity

Solving nonlinear Euler equations is a notoriously challenging task. A smooth solution can turn into a discontinuous one due to nonlinearity. For numerical stability, a sufficient numerical diffusion needs to be equipped 16 17 18

² The Roe average state for \mathbf{q}_{Roe}^* , for example, is defined as $\rho_{Roe}^* = \sqrt{\rho^- \rho^+}$, $\mathbf{u}_{Roe}^* = \frac{\sqrt{\rho^-} \mathbf{u}^- + \sqrt{\rho^+} \mathbf{u}^+}{\sqrt{\rho^-} + \sqrt{\rho^+}}$, $H_{Roe}^* = \frac{\sqrt{\rho^-} H^- + \sqrt{\rho^+} H^+}{\sqrt{\rho^-} + \sqrt{\rho^+}}$, and $a_{Roe}^* = \sqrt{(\gamma-1)(H_{Roe}^* - \frac{1}{2} \|\mathbf{u}_{Roe}^*\|^2)}$.

with the Euler system. The questions are how to measure the regularity of a solution, and how to choose a reasonable amount of the artificial viscosity. The authors in [62,63] introduced entropy viscosity to stabilize numerical solution in Runge Kutta time stepping. Since a large entropy is produced in the vicinity of strong shocks, the size of the entropy residual can be used to measure the solution regularity and the viscosity coefficient.

We employ the entropy viscosity method in the context of exponential DG methods for handling sharp gradient solutions. The procedure is as follows: given an entropy pair $(\mathcal{S}, \mathbf{u}\mathcal{S})$ for Euler systems, we first define the entropy residual, $\mathcal{R}es(\mathbf{q}) := \frac{\partial \mathcal{S}(\mathbf{q})}{\partial t} + \nabla \cdot (\mathbf{u}\mathcal{S}(\mathbf{q}))$, an effective viscosity $\nu_E := c_E h_{max}^2 \max(|\mathcal{R}es|, [\mathbf{u}\mathcal{S}] h^{-1})$, an upper bound to the viscosity $\nu_{max} := c_{max} h_{max} \max|\mathbf{f}'(\mathbf{q})|$ and the entropy viscosity $\nu_{EV} := Smooth(\min(\nu_{max}, \nu_E))$. Here, $\mathcal{S} := \frac{\rho}{\gamma-1} \log\left(\frac{p}{\rho^\gamma}\right)$ is the physical entropy functional for Euler equations; c_E and c_{max} are tunable parameters; h is an element size;³ $\mathbf{f}'(\mathbf{q}) = \frac{\partial \mathbf{f}}{\partial \mathbf{q}}$ is the flux Jacobian; and $Smooth$ is a smooth function.⁴ Then, we add the artificial diffusion term to Euler systems in (14), which leads to

$$\frac{\partial \mathbf{q}}{\partial t} + \nabla \cdot \mathcal{F}(\mathbf{q}) = \nabla \cdot \mathcal{F}^{EV} \quad (16)$$

with $\mathcal{F}^{EV} := (\nu_{EV} \nabla \mathbf{q})$. Note that this choice of the viscous flux makes the diffusion term linear if we compute the entropy viscosity ν_{EV} using the solutions at current and previous timestep.⁵ Thus, the linearized flux in (15) becomes $\mathcal{F}_L := \hat{\mathbf{A}}\mathbf{q} - \nu_{EV} \nabla \mathbf{q}$. Treating the linear diffusion for Euler systems is similar to that for Burgers equation, and hence omitted here.

4. An analysis of the exponential DG method for Burgers equation

In this Section we shall provide a rigorous analysis of the exponential DG approach in Section 2 for the Burger equation (11). For the simplicity of the exposition, we assume that the integrals can be computed exactly though we use LGL quadrature for computing the integrals. Note that aliasing errors from LGL quadrature and interpolation are typically negligible for well-resolved solutions or can be made vanished by using a split form of the flux (see, e.g., [16,64]). For brevity, we assume zero boundary conditions⁶ on both sides of the domain Ω or periodic boundary conditions. Without any ambiguity, we also neglect the dependency of the (semi-discrete and exact) solutions on time t , e.g. $u = u(t)$, except for cases where this dependence is important. We assume that $\kappa > 0$ is a constant. The stability is trivial (see, e.g. [64], and the references therein), thanks to the entropy numerical flux. (Note that unlike the standard entropy numerical flux, ours has an additional jump term.) Indeed, by taking $p = \kappa q$ in (11a) and $v = u$ in (11b), and then adding the resulting equations together we obtain

$$\frac{1}{2} \frac{d}{dt} |u|_{\Omega_h}^2 + \kappa |q|_{\Omega_h}^2 = \left(\frac{1}{6} \frac{\partial u^3}{\partial x}, 1 \right)_{\Omega_h} - \left\langle \left(\frac{u^2}{2} \right)^*, [u] \right\rangle_{\mathcal{E}_h} = -\frac{\sigma}{h} |[u]|_{\mathcal{E}_h}^2. \quad (17)$$

Let us define the DG-norm⁷ for $H^1(\Omega_h)$ as follows

$$|u|_{DG}^2 = \left\| \frac{\partial u}{\partial x} \right\|_{\Omega_h}^2 + \frac{1}{h} |[u]|_{\mathcal{E}_h}^2. \quad (18)$$

Lemma 1 (Semi-discrete Stability and Uniqueness). *The semi-discretization with DG in (11), with $u \in V_h(\Omega_h)$, is stable in the following sense*

$$|u|_{\Omega_h}^2 + C \int_0^t |u|_{DG}^2 d\tau \leq |u(0)|_{\Omega_h}^2,$$

where C is some positive constant and $u(0)$ is the DG initial condition. Hence, the DG solution is unique.

³ We define $h := \frac{2r}{k}$ with $r := \frac{1}{4|K|} \prod_{i=1}^3 s_i$ as the radius of the circumscribed circle on the K th triangular element.

⁴ For smoothing, we first compute vertex averaged entropy viscosity and then linearly reconstruct the entropy viscosity on each element.

⁵ In this study, we approximate the entropy residual by $\mathcal{R}es \approx \frac{\mathcal{S}(\mathbf{q}^n) - \mathcal{S}(\mathbf{q}^{n-1})}{\Delta t} + \frac{1}{2} (\nabla \cdot (\mathbf{u}^n \mathcal{S}(\mathbf{q}^n)) + \nabla \cdot (\mathbf{u}^{n-1} \mathcal{S}(\mathbf{q}^{n-1})))$.

⁶ At the Dirichlet boundary, we take $u^+ = u_D = 0$ for the numerical fluxes $(\tilde{u}u)^*$ and $\left(\frac{u^2}{2}\right)^*$, $u^{**} = u_D = 0$, and $q^{**} = q^-$.

⁷ Recall our convention that on the boundary faces \mathcal{E}_h^∂ we have $[u] = u$. For periodic boundary condition, $|u|_{DG}$ in Lemma 1 and Theorem 1 treats the boundary and interior interfaces the same.

Proof. From an inverse and a multiplicative trace inequalities we have

$$h \left\| \left\{ \left\{ \frac{\partial u}{\partial x} \right\} \right\}_{\mathcal{E}_h} \right\|^2 \leq c_{IT} \left\| \frac{\partial u}{\partial x} \right\|_{\Omega_h}^2, \quad \forall \frac{\partial u}{\partial x} \in V_h(\Omega_h), \quad (19)$$

where c_{IT} is a constant independent of the meshsize h . Taking $p = \frac{\partial u}{\partial x}$ in (11a) we obtain

$$\begin{aligned} \frac{c_1}{2} |q|_{\Omega_h}^2 + \frac{1}{2c_1} \left\| \frac{\partial u}{\partial x} \right\|_{\Omega_h}^2 &\geq \left(q, \frac{\partial u}{\partial x} \right)_{\Omega_h} = \left\| \frac{\partial u}{\partial x} \right\|_{\Omega_h}^2 - \left([u], \left\{ \left\{ \frac{\partial u}{\partial x} \right\} \right\}_{\mathcal{E}_h} \right) \geq \\ &\left\| \frac{\partial u}{\partial x} \right\|_{\Omega_h}^2 - \frac{c_2}{2h} \|[u]\|_{\mathcal{E}_h}^2 - \frac{h}{2c_2} \left\| \left\{ \left\{ \frac{\partial u}{\partial x} \right\} \right\}_{\mathcal{E}_h} \right\|^2 \geq \left(1 - \frac{c_{IT}}{2c_2} \right) \left\| \frac{\partial u}{\partial x} \right\|_{\Omega_h}^2 - \frac{c_2}{2h} \|[u]\|_{\mathcal{E}_h}^2, \end{aligned}$$

where we have used (19) in the third inequality, and c_1, c_2 are arbitrary positive constant. It follows that

$$\frac{c_1}{2} |q|_{\Omega_h}^2 \geq \left(1 - \frac{c_{IT}}{2c_2} - \frac{1}{2c_1} \right) \left\| \frac{\partial u}{\partial x} \right\|_{\Omega_h}^2 - \frac{c_2}{2h} \|[u]\|_{\mathcal{E}_h}^2,$$

which, together with (17), yields

$$\frac{d}{dt} |u|_{\Omega_h}^2 + \frac{2\kappa}{c_1} \left(2 - \frac{c_{IT}}{c_2} - \frac{1}{c_1} \right) \left\| \frac{\partial u}{\partial x} \right\|_{\Omega_h}^2 + \frac{2}{h} \left(\sigma - \frac{\kappa c_2}{c_1} \right) \|[u]\|_{\mathcal{E}_h}^2 \leq 0.$$

Now, by choosing c_1, c_2 large enough such that

$$\sigma - \frac{\kappa c_2}{c_1} > 0, \quad \text{and} \quad 2 - \frac{c_{IT}}{c_2} - \frac{1}{c_1} > 0,$$

and defining

$$C := \min \left\{ \sigma - \frac{\kappa c_2}{c_1}, 2 - \frac{c_{IT}}{c_2} - \frac{1}{c_1} \right\},$$

we arrive at

$$\frac{d}{dt} |u|_{\Omega_h}^2 + C |u|_{DG}^2 \leq 0,$$

which concludes the proof. \square

Remark 1. We can choose c_1 sufficiently large relative to κc_2 so that σ can be chosen to be (very) small.

Note that the L^2 -stability in Lemma 1 does not imply L^∞ -stability in general. The fact that $V_h(\Omega_h)$ is piecewise continuous implies⁸ $V_h(\Omega_h) \subset L^\infty(\Omega_h)$, i.e., $|u|_\infty < \infty$. For the convergence analysis, we assume that $|u|_\infty$ is bounded uniformly for the time horizon $(0, T)$, i.e., there exists $M < \infty$ so that $|u|_\infty \leq M$ at any $t \in (0, T)$. Let us denote by \hat{u} and $\hat{q} = \frac{\partial \hat{u}}{\partial x}$ the exact solution and its gradient, and we assume that $\hat{u}, \frac{\partial \hat{u}}{\partial x} \in H^s(\Omega)$ with $s > 3/2$ for $t \in (0, T)$. By the Sobolev embedding theorem, \hat{u} and \hat{q} are continuous and without loss of generality we assume $\|\hat{u}\|_\infty \leq M$. It is easy to see that \hat{u} and \hat{q} satisfy the DG weak form (11). Let Π be the L^2 -projection onto $V_h(\Omega_h)$ and let us define

$$\begin{aligned} \varepsilon_u &:= \hat{u} - u = \underbrace{\hat{u} - \Pi \hat{u}}_{=: \varepsilon_u^I} + \underbrace{\Pi \hat{u} - u}_{=: \varepsilon_u^h} = \varepsilon_u^I + \varepsilon_u^h, \\ \varepsilon_q &:= \hat{q} - q = \underbrace{\hat{q} - \Pi \hat{q}}_{=: \varepsilon_q^I} + \underbrace{\Pi \hat{q} - q}_{=: \varepsilon_q^h} = \varepsilon_q^I + \varepsilon_q^h. \end{aligned}$$

⁸ In fact, by an inverse inequality and shape regularity, we can obtain the estimate $|u|_\infty \leq Ch^{-1} |u|_{\Omega_h}$.

Since both the exact and the DG solutions satisfy the DG weak form (11), we subtract their corresponding equations, take $v = \varepsilon_u^h$ and $p = \kappa \varepsilon_q^h$, and add the resulting equations altogether to obtain

$$\begin{aligned}
 \frac{1}{2} \frac{d}{dt} \|\varepsilon_u^h\|_{\Omega_h}^2 + \underbrace{\kappa \|\varepsilon_q^h\|_{\Omega_h}^2}_{E_1} &= \underbrace{-\kappa (\varepsilon_q^I, \varepsilon_q^h)_{\Omega_h} + \kappa \left(\frac{\partial \varepsilon_u^I}{\partial x}, \varepsilon_q^h \right)_{\Omega_h}}_{E_2} - \kappa \langle [\varepsilon_u^I], \{\varepsilon_q^h\} \rangle_{\varepsilon_h} \\
 &\quad - \underbrace{\kappa \left(\varepsilon_q^I, \frac{\partial \varepsilon_u^h}{\partial x} \right)_{\Omega_h}}_{E_3} + \underbrace{\kappa \langle \{\varepsilon_q^I\}, [\varepsilon_u^h] \rangle_{\varepsilon_h}}_{E_4} - \underbrace{\left(\frac{\partial \varepsilon_u^I}{\partial t}, \varepsilon_u^h \right)_{\Omega_h}}_{E_4} \\
 &\quad + \underbrace{\left(\frac{\hat{u}^2 - u^2}{2}, \frac{\partial \varepsilon_u^h}{\partial x} \right)_{\Omega_h} - \left\langle \left(\frac{\hat{u}^2}{2} \right)^* - \left(\frac{u^2}{2} \right)^*, [\varepsilon_u^h] \right\rangle_{\varepsilon_h}}_{E_5}. \tag{20}
 \end{aligned}$$

Lemma 2 (Estimate for E_1). Assume that the mesh Ω_h is regular. There holds:

$$E_1 \geq \frac{1}{c_1} \left(2 - \frac{1}{c_1} - \frac{c_{IT}}{c_2} \right) \left\| \frac{\partial \varepsilon_u^h}{\partial x} \right\|_{\Omega_h}^2 - \frac{c_2}{hc_1} \|\llbracket \varepsilon_u^h \rrbracket\|_{\varepsilon_h}^2 + \underbrace{\frac{2}{c_1} \left(\frac{\partial \varepsilon_u^I}{\partial x} - \varepsilon_q^I, \frac{\partial \varepsilon_u^h}{\partial x} \right)_{\Omega_h}}_{E_3^b} - \frac{2}{c_1} \langle [\varepsilon_u^I], \left\{ \left\{ \frac{\partial \varepsilon_u^h}{\partial x} \right\} \right\} \rangle_{\varepsilon_h}$$

Proof. Since both the exact and DG solutions satisfy (11a), taking $p = \frac{\partial \varepsilon_u^h}{\partial x}$ in (11a) yields

$$\begin{aligned}
 \frac{c_1}{2} \|\varepsilon_q^h\|_{\Omega_h}^2 + \frac{1}{2c_1} \left\| \frac{\partial \varepsilon_u^h}{\partial x} \right\|_{\Omega_h}^2 &\geq \left(\varepsilon_q^h, \frac{\partial \varepsilon_u^h}{\partial x} \right)_{\Omega_h} = \left\| \frac{\partial \varepsilon_u^h}{\partial x} \right\|_{\Omega_h}^2 - \langle [\varepsilon_u^h], \left\{ \left\{ \frac{\partial \varepsilon_u^h}{\partial x} \right\} \right\} \rangle_{\varepsilon_h} \\
 &\quad - \left(\varepsilon_q^I, \frac{\partial \varepsilon_u^h}{\partial x} \right)_{\Omega_h} + \left(\frac{\partial \varepsilon_u^I}{\partial x}, \frac{\partial \varepsilon_u^h}{\partial x} \right)_{\Omega_h} - \langle [\varepsilon_u^I], \left\{ \left\{ \frac{\partial \varepsilon_u^h}{\partial x} \right\} \right\} \rangle_{\varepsilon_h}.
 \end{aligned}$$

Now using Cauchy–Schwarz we have

$$\langle [\varepsilon_u^h], \left\{ \left\{ \frac{\partial \varepsilon_u^h}{\partial x} \right\} \right\} \rangle_{\varepsilon_h} \leq \frac{c_{IT}}{2c_2} \left\| \frac{\partial \varepsilon_u^h}{\partial x} \right\|_{\Omega_h}^2 + \frac{c_2}{2h} \|\llbracket \varepsilon_u^h \rrbracket\|_{\varepsilon_h}^2,$$

where c_{IT} , independent of h , is constant resulting from the inverse and multiplicative trace inequalities (19). Now combining the two inequalities ends the proof. \square

Lemma 3 (Estimate for E_2). Assume that the mesh Ω_h is regular. There holds:

$$\frac{E_2}{\kappa} \leq \frac{c_1^q}{2} \|\varepsilon_q^I\|_{\Omega_h}^2 + \frac{c_2^q}{2} \left\| \frac{\partial \varepsilon_u^I}{\partial x} \right\|_{\Omega_h}^2 + \frac{c_1^u}{2h} \|\llbracket \varepsilon_u^I \rrbracket\|_{\varepsilon_h}^2 + \frac{1}{2} \left(\frac{1}{c_1^q} + \frac{1}{c_2^q} + \frac{c_{IT}}{c_1^u} \right) \|\varepsilon_q^h\|_{\Omega_h}^2,$$

where c_{IT} , independent of h , is constant resulting from an inverse and multiplicative trace inequalities, while c_1^q , c_2^q and c_1^u are any positive constants.

Proof. The proof is straightforward using a Cauchy–Schwarz, an inverse, and multiplicative trace inequalities. \square

Lemma 4 (Estimate for $E_3^a - E_3^b/2$). Assume that the mesh Ω_h is regular. There holds:

$$\begin{aligned} E_3^a - E_3^b/2 &\leq \left(\frac{c_2^u (\kappa - 2)}{2} + \frac{\kappa c_{IT} c_3^u}{2} \right) \|\varepsilon_q^I\|_{\Omega_h}^2 + \frac{c_4^u}{2c_1^2} \left\| \frac{\partial \varepsilon_u^I}{\partial x} - \varepsilon_q^I \right\|_{\Omega_h}^2 + \frac{c_5^u}{2hc_1^2} \|[\varepsilon_u^I]\|_{\varepsilon_h}^2 \\ &\quad + \left(\frac{\kappa - 2}{2c_2^u} + \frac{1}{2c_4^u} + \frac{c_{IT}}{2c_5^u} \right) \left\| \frac{\partial \varepsilon_u^h}{\partial x} \right\|_{\Omega_h}^2 + \frac{\kappa}{2hc_3^u} \|[\varepsilon_u^h]\|_{\varepsilon_h}^2, \end{aligned}$$

where c_{IT} , independent of h , is constant resulting from an inverse and a multiplicative trace inequalities, while c_2^u, c_3^u, c_4^u and c_5^u are any positive constants.

Proof. The proof is straightforward using a Cauchy–Schwarz, and an inverse and a multiplicative trace inequality similar to (19). \square

Lemma 5 (Estimate for E_4). Assume that the mesh Ω_h is regular. There holds:

$$E_4 \leq \frac{c_6^u}{2} \left\| \frac{\partial \varepsilon_u^I}{\partial t} \right\|_{\Omega_h}^2 + \frac{1}{2c_6^u} \|\varepsilon_u^h\|_{\Omega_h}^2.$$

where c_6^u is any positive constant.

Lemma 6 (Estimate for E_5). Assume that the mesh Ω_h is regular, $\|\hat{u}\|_{\infty} \leq M$, and $|u|_{\infty} \leq M$ over the time horizon of interest. There holds:

$$\begin{aligned} E_5 &\leq \frac{M c_{IT} c_8^u}{2} \left(\|\varepsilon_u^I\|_{\Omega_h}^2 + h^2 \left\| \frac{\partial \varepsilon_u^I}{\partial x} \right\|_{\Omega_h}^2 \right) + \frac{\sigma c_7^u}{2h} \|[\varepsilon_u^I]\|_{\varepsilon_h}^2 + \frac{M}{c_8^u} \|\varepsilon_u^h\|_{DG}^2 \\ &\quad + \frac{M c_{IT} c_8^u}{2} \|\varepsilon_u^h\|_{\Omega_h}^2 + \frac{\sigma}{h} \left(\frac{1}{2c_7^u} - 1 \right) \|[\varepsilon_u^h]\|_{\varepsilon_h}^2, \end{aligned}$$

where c_7^u and c_8^u are any positive constant.

Proof. We begin with the Lipschitz continuity of the flux function and the numerical flux

$$\frac{1}{2} (\hat{u}^2 - u^2) \leq M |\varepsilon_u|, \quad \text{and} \quad \left(\frac{\hat{u}^2}{2} \right)^* - \left(\frac{u^2}{2} \right)^* \leq M (|\varepsilon_u^+| + |\varepsilon_u^-|) + \frac{\sigma}{h} [\varepsilon_u],$$

and thus by Cauchy–Schwarz inequality we have

$$E_5 \leq \underbrace{M \left(|\varepsilon_u^I|, \left| \frac{\partial \varepsilon_u^h}{\partial x} \right| \right)_{\Omega_h} + M (|\varepsilon_{u^+}^I| + |\varepsilon_{u^-}^I|, |[\varepsilon_u^h]|)_{\varepsilon_h}}_{B(\varepsilon_u^I, \varepsilon_u^h)}$$

$$+ \underbrace{M \left(|\varepsilon_u^h|, \left| \frac{\partial \varepsilon_u^h}{\partial x} \right| \right)_{\Omega_h} + M (|\varepsilon_{u^+}^h| + |\varepsilon_{u^-}^h|, |[\varepsilon_u^h]|)_{\varepsilon_h}}_{B(\varepsilon_u^h, \varepsilon_u^h)}$$

$$+ \frac{\sigma c_7^u}{2h} \|[\varepsilon_u^I]\|_{\varepsilon_h}^2 + \frac{\sigma}{h} \left(\frac{1}{2c_7^u} - 1 \right) \|[\varepsilon_u^h]\|_{\varepsilon_h}^2,$$

where we have defined $\varepsilon_{u^\pm}^h := (\varepsilon_u^h)^\pm$.

1 To estimate $B(\varepsilon_u^I, \varepsilon_u^h)$ we apply Cauchy–Schwarz inequality and a multiplicative trace inequality to obtain

$$\begin{aligned}
 2 \quad B(\varepsilon_u^I, \varepsilon_u^h) &\leq M \left(\|\varepsilon_u^I\|_{\Omega_h}^2 + h \|\varepsilon_u^I\|_{\varepsilon_h}^2 \right)^{\frac{1}{2}} \|\varepsilon_u^h\|_{DG} \\
 3 \quad &\leq \frac{M c_8^u}{2} \left(\|\varepsilon_u^I\|_{\Omega_h}^2 + h \|\varepsilon_u^I\|_{\varepsilon_h}^2 \right) + \frac{M}{2 c_8^u} \|\varepsilon_u^h\|_{DG}^2 \\
 4 \quad &\leq \frac{M c_{IT} c_8^u}{2} \left(\|\varepsilon_u^I\|_{\Omega_h}^2 + h^2 \left\| \frac{\partial \varepsilon_u^I}{\partial x} \right\|_{\Omega_h}^2 \right) + \frac{M}{2 c_8^u} \|\varepsilon_u^h\|_{DG}^2.
 \end{aligned}$$

5 Similarly, together with an inverse inequality, we have

$$6 \quad B(\varepsilon_u^h, \varepsilon_u^I) \leq \frac{M c_8^u}{2} \left(\|\varepsilon_u^h\|_{\Omega_h}^2 + h \|\varepsilon_u^h\|_{\varepsilon_h}^2 \right) + \frac{M}{2 c_8^u} \|\varepsilon_u^h\|_{DG}^2 \leq \frac{M c_{IT} c_8^u}{2} \|\varepsilon_u^h\|_{\Omega_h}^2 + \frac{M}{2 c_8^u} \|\varepsilon_u^h\|_{DG}^2.$$

7 Combining the above estimates concludes the proof. \square

Now combining Lemmas 2–6 and (20) we arrive at

$$\begin{aligned}
 \frac{d}{dt} \|\varepsilon_u^h\|_{\Omega_h}^2 + C_1 \|\varepsilon_q^h\|_{\Omega_h}^2 + C_2 \|\varepsilon_u^h\|_{DG}^2 &\leq M c_{IT} c_8^u \left(\|\varepsilon_u^I\|_{\Omega_h}^2 + h^2 \left\| \frac{\partial \varepsilon_u^I}{\partial x} \right\|_{\Omega_h}^2 \right) \\
 &\quad + (\kappa c_1^q + c_2^u (\kappa - 2) + \kappa c_{IT} c_3^u + 2c_4^u) \|\varepsilon_q^I\|_{\Omega_h}^2 + (\kappa c_2^q + 2c_4^u) \left\| \frac{\partial \varepsilon_u^I}{\partial x} \right\|_{\Omega_h}^2 \\
 &\quad + c_6^u \left\| \frac{\partial \varepsilon_u^I}{\partial t} \right\|_{\Omega_h}^2 + (\kappa c_1^u + c_5^u + \sigma c_7^u) \frac{1}{h} \|\varepsilon_u^I\|_{\varepsilon_h}^2 + C_3 \|\varepsilon_u^h\|_{\Omega_h}^2, \quad (21)
 \end{aligned}$$

where we have defined

$$\begin{aligned}
 C_1 &:= \frac{2\kappa}{c_1} \left(2 - \frac{1}{c_1} - \frac{c_{IT}}{c_2} \right) - \frac{1}{c_1^q} - \frac{1}{c_2^q} - \frac{c_{IT}}{c_1^u}, \\
 C_2^1 &:= \left(\frac{\kappa}{2} - \frac{\kappa - 2}{c_2^u} - \frac{2}{c_4^u} - \frac{c_{IT}}{c_5^u} - \frac{2M}{c_8^u} \right), \\
 C_2^2 &:= \sigma \left(1 - \frac{1}{c_7^u} \right) - \frac{\kappa}{c_3^u} - \frac{2M}{c_8^u} - \frac{2\kappa c_2}{c_1}, \\
 C_2 &:= \min \{ C_2^1, C_2^2 \}, \\
 C_3 &:= \left(\frac{1}{c_6^u} + M c_{IT} c_8^u \right).
 \end{aligned}$$

10 As can be seen, for a given κ , we can choose $c_1, c_2, \sigma, c_1^q, c_2^q$, and $c_i^u, i = 1, \dots, 8$ such that all the constants
 11 C_1, C_2 and C_3 are positive.

12 **Theorem 1** (Semi-discrete Error Estimate). Assume $\hat{u}, \frac{\partial \hat{u}}{\partial t} \in H^s(\Omega)$ with $s > 3/2$ for $t \in [0, T]$, and $\sigma > 0$. There
 13 exist positive constants C independent of the meshsize h and t such that

$$14 \quad \frac{d}{dt} \|\varepsilon_u^h\|_{\Omega_h}^2 + \|\varepsilon_q^h\|_{\Omega_h}^2 + \|\varepsilon_u^h\|_{DG}^2 \leq C \|\varepsilon_u^I\|_{\Omega_h}^2 + C h^{2\min\{s,k\}} \left(\|\hat{u}\|_{H^s(\Omega)}^2 + \left\| \frac{\partial \hat{u}}{\partial t} \right\|_{H^s(\Omega)}^2 \right), \quad (22)$$

15 and thus, in addition, if $\hat{u}, \frac{\partial \hat{u}}{\partial t} \in L^2((0, T); H^s(\Omega))$ and $u(0) = \Pi \hat{u}(0)$, there exists a constant C independent of
 16 the meshsize h and t such that

$$17 \quad \|\varepsilon_u\|_{\Omega_h}^2 + \int_0^t \left(\|\varepsilon_q\|_{\Omega_h}^2 + \|\varepsilon_u\|_{DG}^2 \right) ds \leq C h^{2\min\{s,k\}} (\exp(Ct) - 1).$$

18

Proof. The first assertion is the direct consequence of the error estimation (21), the L^2 -projection error [65–69], and the following definition of C :

$$C := \max \left\{ \frac{C_3}{\min \{1, C_1, C_2\}}, \frac{C_4}{\min \{1, C_1, C_2\}} \right\}.$$

The second assertion is straightforward by (1) integrating the first assertion and then applying a Gronwall's lemma to obtain,

$$\|\varepsilon_u^h\|_{\Omega_h}^2 + \int_0^t \left(\|\varepsilon_q^h\|_{\Omega_h}^2 + \|\varepsilon_u^h\|_{DG}^2 \right) ds \leq Ch^{2\min\{s,k\}} (\exp(Ct) - 1) \int_0^t \left(\|\hat{u}\|_{H^s(\Omega)}^2 + \left\| \frac{\partial \hat{u}}{\partial t} \right\|_{H^s(\Omega)}^2 \right) ds.$$

and (2) using the L^2 -projection error [65–69] and triangle inequalities for ε_u and ε_q , e.g.,

$$\|\varepsilon_u\|_{\Omega_h} \leq \|\varepsilon_u^f\|_{\Omega_h} + \|\varepsilon_u^h\|_{\Omega_h}. \quad \square$$

Remark 2. Theorem 1 shows that though the convergence of the solution in the DG norm (18) is optimal, the convergence in L^2 -error is suboptimal, i.e. $\|\varepsilon_u\|_{\Omega_h} = \mathcal{O}(h^k)$ if $k \leq s$, and this seems to be sharp as we observe this rate in the diffusion-dominated numerical results especially for odd k . When $Ct \ll 1$, then $\exp(Ct) - 1 \approx Ct$, and thus the error increases at most linearly in time.

We next analyze the temporal discretization error using the exponential integrator. We begin with a few important lemmas.

Lemma 7. *There exists a constant C , independent of the meshsize h , such that:*

$$h \|\{q\}\|_{\varepsilon_h}^2 + |q|_{\Omega_h}^2 \leq C \|u\|_{DG}^2$$

Proof. Taking $p = q$ in (11a), then using Cauchy–Schwarz and multiplicative trace and inverse inequality similar to (19) give

$$\begin{aligned} \frac{h}{4c_{IT}} \|\{q\}\|_{\varepsilon_h}^2 + \frac{3}{4} |q|_{\Omega_h}^2 &\leq |q|_{\Omega_h}^2 = \left(\frac{\partial u}{\partial x}, q \right)_{\Omega_h} - \langle [u], \{q\} \rangle_{\varepsilon_h} \\ &\leq \frac{1}{2} \left\| \frac{\partial u}{\partial x} \right\|_{\Omega_h}^2 + \frac{1}{2} |q|_{\Omega_h}^2 + \frac{2c_{IT}}{h} \|[u]\|_{\varepsilon_h}^2 + \frac{h}{8c_{IT}} \|\{q\}\|_{\varepsilon_h}^2, \end{aligned}$$

then taking $C = \max \left\{ \frac{1}{2}, 2c_{IT} \right\} / \min \left\{ \frac{1}{8c_{IT}}, \frac{1}{4} \right\}$ concludes the proof. \square

Using the definition of the L^2 -projection, e.g., $\Pi \mathcal{N}(u) \in V_h(\Omega_h)$ such that $\langle \mathcal{N}(u), v \rangle = \langle \Pi \mathcal{N}(u), v \rangle_{\Omega_h}$ for all $v \in V_h(\Omega_h)$, we can write (11b) as

$$\frac{\partial u}{\partial t} = \Pi L u + \Pi \mathcal{N}(u).$$

For the clarity of the exposition let us define $\mathbb{L} := \Pi L$ and $\mathbb{N} := \Pi \mathcal{N}$. For the rest of the analysis, we do not distinguish the operator $\mathbb{L}u$ (and hence $\mathbb{N}(u)$) and its matrix representation from $V_h(\Omega_h)$ to $V_h(\Omega_h)$ since in finite dimension all norms are equivalent and $V_h(\Omega_h)$ is homeomorphic to \mathbb{R}^M , where M is the dimension of $V_h(\Omega_h)$. This allows us to work conveniently and directly on \mathbb{L} , \mathbb{N} , $V_h(\Omega_h)$, and the DG-norm.

Lemma 8 (Uniform Boundedness of L and \mathbb{L} on $V_h(\Omega_h)$). *Suppose that $\|\tilde{u}\|_{\infty} \leq M$, the linear operator \mathbb{L} defined in (11b), as a linear operator from $V_h(\Omega_h)$ to $V_h(\Omega_h)$, is bounded for any $t \in (0, T)$ in the following sense: there exists a constant C_L , independent of the meshsize h , u , v , such that*

$$\|(\mathbb{L}u, v)_{\Omega_h}\| = |\langle Lu, v \rangle| \leq C_L \|u\|_{DG} \|v\|_{DG}, \quad \forall u, v \in V_h(\Omega_h).$$

Proof. We have

$$\begin{aligned} \langle \mathbf{n}(\tilde{u}u)^*, v \rangle_{\partial\Omega_h} &\leq M \langle |u|, |[v]| \rangle_{\partial\Omega_h}, \text{ and } \langle \mathbf{n}\kappa q^{**}, v \rangle_{\partial\Omega_h} \leq \kappa \langle |\{q\}|, |[v]| \rangle_{\mathcal{E}_h}, \\ \left(\kappa q - \tilde{u}u, \frac{\partial v}{\partial x} \right)_{\Omega_h} &\leq \kappa \left(|q|, \left| \frac{\partial v}{\partial x} \right| \right)_{\Omega_h} + \kappa M \left(|u|, \left| \frac{\partial v}{\partial x} \right| \right)_{\Omega_h}. \end{aligned}$$

1 Now from definition of L in (12a) using Cauchy–Schwarz inequality we obtain

$$\begin{aligned} \langle Lu, v \rangle^2 &\leq \left(\frac{\kappa M}{2} |u|_{\Omega_h}^2 + \frac{\beta h}{2} |u|_{\partial\Omega_h}^2 + \frac{\kappa}{2} |q|_{\Omega_h}^2 + \frac{\kappa h}{2} |\{q\}|_{\mathcal{E}_h}^2 \right) \\ &\times \left(\frac{\kappa M}{2} \left\| \frac{\partial v}{\partial x} \right\|_{\Omega_h}^2 + \frac{\beta}{h} |[v]|_{\mathcal{E}_h}^2 + \frac{\kappa}{2} \left\| \frac{\partial v}{\partial x} \right\|_{\Omega_h}^2 + \frac{\kappa}{2h} |[v]|_{\mathcal{E}_h}^2 \right), \end{aligned}$$

3 Now using the result of Lemma 7, a Poincaré–Friedrichs inequality for $H^1(\Omega_h)$, and a multiplicative trace inequality
4 for $|u|_{\mathcal{E}_h}$ we arrive at

$$\langle Lu, v \rangle^2 \leq \left[C_{PF} \left(\frac{\kappa M}{2} + \frac{\beta c_{IT}}{2} \right) + \frac{\kappa C}{2} \right] |u|_{DG}^2 \times \max \left\{ \frac{\kappa M}{2} + \frac{\kappa}{2}, \beta + \frac{\kappa}{2} \right\} |v|_{DG}^2,$$

6 where C_{PF} is the constant in the Poincaré–Friedrichs inequality. The result follows by taking

$$C_L^2 := \left[C_{PF} \left(\frac{\kappa M}{2} + \frac{\beta c_{IT}}{2} \right) + \frac{\kappa C}{2} \right] \times \max \left\{ \frac{\kappa M}{2} + \frac{\kappa}{2}, \beta + \frac{\kappa}{2} \right\}. \quad \square$$

8 **Corollary 1.** Suppose the assumptions for Lemma 8 hold. We have that

$$e^{t\mathbb{L}} := \sum_{m=0}^{\infty} \frac{(t\mathbb{L})^m}{m!}, \quad t \geq 0,$$

10 is a uniform continuous operator semigroup in $V_h(\Omega_h)$. In particular, \mathbb{L} is the infinitesimal generator of the
11 semigroup $e^{t\mathbb{L}}$ with

$$\|e^{t\mathbb{L}}\| \leq e^{C_L t} \text{ and } \|\varphi_i(\tau\mathbb{L})\| \leq C_{\varphi_i}(\tau) := e^{\tau C_L} \int_0^1 \frac{z^{i-1}}{(i-1)!} dz,$$

13 where $\|\cdot\|$ is the operator norm from $V_h(\Omega_h)$ to $V_h(\Omega_h)$.

14 **Proof.** The proof is straightforward using the boundedness of \mathbb{L} in Lemma 8 [70,71]. \square

15 **Lemma 9** (Lipschitz Continuity of \mathcal{N}). Let u and w be in $V_h(\Omega_h)$, $|u|_{\infty} \leq M$ and $|w|_{\infty} \leq M$ for $t \in (0, T)$, there
16 exists a constant $C_{\mathcal{N}}$ independent of the meshsize such that

$$|\langle \mathcal{N}(u) - \mathcal{N}(w), v \rangle| \leq C_{\mathcal{N}} |u - w|_{DG} |v|_{DG}, \quad \forall v \in V_h(\Omega_h).$$

18

Proof. From the definition of \mathcal{N} in (12b), it is easy to see that

$$\begin{aligned} \left(\frac{u^2}{2} \right)^* - \left(\frac{w^2}{2} \right)^* &\leq \frac{M}{3} (|u^- - w^-| + |u^+ - w^+|) + \frac{\sigma}{h} [u - w], \\ (\tilde{u}u)^* - (\tilde{w}w)^* &\leq 2M (|u^- - w^-| + |u^+ - w^+|), \\ \left(\tilde{u}u - \frac{1}{2}u^2 \right) - \left(\tilde{w}w - \frac{1}{2}w^2 \right) &\leq 2M |u - w|. \end{aligned}$$

19 Thus,

$$\begin{aligned} |\langle \mathcal{N}(u) - \mathcal{N}(w), v \rangle| &\leq 2M |u - w|_{\Omega_h} \left\| \frac{\partial v}{\partial x} \right\|_{\Omega_h} + \frac{7M}{3} |u - w|_{\partial\Omega_h} |[v]|_{\mathcal{E}_h} \\ &\quad + \frac{\sigma}{h} |[u - w]|_{\mathcal{E}_h} |[v]|_{\mathcal{E}_h} \end{aligned}$$

21

$$\leq \left[M^2 \left(4 + \frac{98}{9} c_{IT} \right) |u - w|_{\Omega_h}^2 + \frac{2\sigma^2}{h} \|[u - w]\|_{\mathcal{E}_h}^2 \right]^{\frac{1}{2}} |v|_{DG} \quad 1$$

$$\leq \underbrace{\left[C_{PF} M^2 \left(4 + \frac{98}{9} c_{IT} \right) + 2\sigma^2 \right]^{\frac{1}{2}}}_{C_{\mathcal{N}}} |u - w|_{DG} |v|_{DG}, \quad 2$$

where we have used Cauchy–Schwarz, inverse trace, and Poincaré–Friedrichs inequalities. \square 3

A direct consequence of [Lemmas 8](#) and [9](#) is that $\frac{\partial u}{\partial t} = \mathbb{L}u + \mathbb{N}(u) \in V_h(\Omega_h) \subset L^\infty(\Omega_h)$. Thus from [\(12b\)](#), $\frac{\partial \mathbb{N}}{\partial t}$ 4
given by 5

$$\left\langle \frac{\partial \mathbb{N}(u)}{\partial t}, v \right\rangle := \left((u - \tilde{u}) \frac{\partial u}{\partial t}, \frac{\partial v}{\partial t} \right)_{\Omega_h} + \left\langle \left\{ \tilde{u} \frac{\partial u}{\partial t} \right\} + \frac{1}{2} \max(|\tilde{u}^\pm|) \left[\frac{\partial u}{\partial t} \right], [v] \right\rangle_{\mathcal{E}_h} \quad 6$$

$$- \left\langle \frac{1}{3} \left\{ u \frac{\partial u}{\partial t} \right\} + \frac{2}{3} \{u\} \left\{ \frac{\partial u}{\partial t} \right\} + \frac{\sigma}{h} \left[\frac{\partial u}{\partial t} \right], [v] \right\rangle_{\mathcal{E}_h} \quad 6$$

is well-defined. Indeed the next results show that $\frac{\partial \mathbb{N}}{\partial t}$ is a Lipschitz continuous map from $V_h(\Omega_h)$ to $V_h(\Omega_h)$. 7

Lemma 10 (Lipschitz Continuity of $\frac{\partial \mathbb{N}}{\partial t}$). Suppose $u, \frac{\partial u}{\partial t}, \tilde{u}, w$ reside in $V_h(\Omega_h)$, $|u|_\infty \leq M$, $|w|_\infty \leq M$, $|\tilde{u}|_\infty \leq M$, 8
and $\left\| \frac{\partial u}{\partial t} \right\|_\infty \leq M$ for $t \in (0, T)$. There exists a constant $C'_{\mathcal{N}}$ independent of the mesh size h such that 9

$$\left| \left\langle \frac{\partial \mathbb{N}(u)}{\partial t} - \frac{\partial \mathbb{N}(w)}{\partial t}, v \right\rangle \right| \leq C'_{\mathcal{N}} |u - w|_{DG} |v|_{DG} \quad 10$$

11

Proof. Let us define z as 12

$$z := \frac{\partial u}{\partial t} - \frac{\partial w}{\partial t} = \mathbb{L}(u - w) + \mathbb{N}(u) - \mathbb{N}(w), \quad 13$$

and [Lemmas 8](#) and [9](#) imply $|z|_{DG} \leq (C_L + C_{\mathcal{N}}) |u - w|_{DG}$. We have 14

$$\langle T, v \rangle = \left((u - w) \frac{\partial u}{\partial t} + (w - \tilde{u}) z, \frac{\partial v}{\partial t} \right)_{\Omega_h} + \left\langle \left\{ \tilde{u} z \right\} + \frac{1}{2} \max(|\tilde{u}^\pm|) [z], [v] \right\rangle_{\mathcal{E}_h} \quad 15$$

$$- \left\langle \frac{1}{3} \left\{ (u - w) \frac{\partial u}{\partial t} + w z \right\} + \frac{2}{3} \{u - w\} \left\{ \frac{\partial u}{\partial t} \right\} + \frac{2}{3} \{w\} \{z\} + \frac{\sigma}{h} [z], [v] \right\rangle_{\mathcal{E}_h}, \quad 16$$

where $T := \frac{\partial \mathbb{N}(u)}{\partial t} - \frac{\partial \mathbb{N}(w)}{\partial t}$. Now following similar arguments as in the proof of [Lemma 9](#) we obtain 17

$$\langle T, v \rangle \leq C |z|_{DG} |v|_{DG} \leq C (C_L + C_{\mathcal{N}}) |u - w|_{DG} |v|_{DG}, \quad 18$$

where $C = C(c_{IT}, M, \sigma, C_{PF})$. \square 19

Let us denote by u^n the approximation solution of [\(11\)](#) using a time discretization. We are now in the position to 20
analyze error of the fully discrete system using the exponential-Euler in time and DG in space. The fully discrete 21
system using the exponential Euler integrator reads 22

$$u^{n+1} := e^{\Delta t \mathbb{L}} u^n + \Delta t \varphi_1(\Delta t \mathbb{L}) \mathbb{N}(u^n), \quad 23$$

while the semi-discrete solution $u(t^n)$ satisfies 24

$$u(t^{n+1}) = e^{\Delta t \mathbb{L}} u(t^n) + \Delta t \varphi_1(\Delta t \mathbb{L}) \mathbb{N}(u(t^n)) + \delta^{n+1}, \quad 25$$

1 with

$$2 \quad \delta^{n+1} := \int_0^{\Delta t} e^{(\Delta t - \tau)L} \int_0^\tau \frac{\partial \mathbb{N}}{\partial t} (u(t^n + \theta)) d\theta d\tau.$$

3 Let us define⁹

$$4 \quad \xi^n := \hat{u}(t^n) - u^n = \underbrace{\hat{u}(t^n) - u(t^n)}_{\varepsilon_u(t^n)} + \underbrace{u(t^n) - u^n}_{=: \rho^n} = \varepsilon_u(t^n) + \rho^n.$$

5 We thus have

$$6 \quad \rho^{n+1} = e^{\Delta t \mathbb{L}} \rho^n + \Delta t \varphi_1(\Delta t \mathbb{L}) \underbrace{[\mathbb{N}(u(t^n)) - \mathbb{N}(u^n)]}_{=: f(t^n)} + \delta^{n+1}.$$

7 After some algebraic manipulations we obtain

$$8 \quad \rho^n = \Delta t \sum_{j=0}^{n-1} e^{(n-j-1)\Delta t \mathbb{L}} \varphi_1(\Delta t \mathbb{L}) f(t_j) + \sum_{j=0}^{n-1} e^{j\Delta t \mathbb{L}} \delta^{n-j}.$$

9 **Theorem 2** (Convergence of the Exponential Euler-DG). Assume the conditions of [Corollary 1](#), [Lemmas 10, 9, 1](#),
10 and [Theorem 1](#) hold. There exists a constant C depending only on t^n , C_L , $C_{\mathcal{N}}$, $\|u(0)\|_{\Omega_h}$, C_{PF} such that the following
11 estimate for the total discrete error ξ^n at $t^n = n\Delta t$ holds true:

$$12 \quad \|\xi^n\|_{\Omega_h} \leq C (\Delta t + h^{\min\{s,k\}}).$$

13
14 **Proof.** Using [Corollary 1](#), [Lemmas 10](#), and [1](#) we have

$$15 \quad \left\| \sum_{j=0}^{n-1} e^{j\Delta t \mathbb{L}} \delta^{n-j} \right\|_{DG} \leq \Delta t e^{t^n C_L} C'_{\mathcal{N}} \sum_{j=1}^n \int_{t^{j-1}}^{t^j} |u(t)|_{DG} dt \\ \leq \Delta t \sqrt{t^n} e^{t^n C_L} C'_{\mathcal{N}} \sqrt{\int_0^{t^n} |u(t)|_{DG}^2 dt} \leq \Delta t C \underbrace{\|u(0)\|_{\Omega_h}}_{C_\delta}$$

16 where we have absorbed all quantities depending only on t^n , C_L , $C_{\mathcal{N}}$ into C . Now combining the above estimate
17 with Lipschitz continuity of \mathbb{N} ([Lemma 9](#)) and [Corollary 1](#) we have that there exists a constant C_1 depending on
18 $C_{\varphi_1}(\Delta t)$ and C_δ such that

$$19 \quad \|\rho^n\|_{DG} \leq C_1 \Delta t \sum_{j=0}^{n-1} \|\rho^j\|_{DG} + C_1 \Delta t,$$

20 which, together with a discrete Gronwall's lemma, yield

$$21 \quad \|\rho^n\|_{\Omega_h} \leq C_{PF} \|\rho^n\|_{DG} \leq C \Delta t,$$

22 where $C = C(C_{PF}, C_1)$. We thus, via [Theorem 1](#), conclude

$$23 \quad \|\xi^n\|_{\Omega_h} \leq \|\rho^n\|_{\Omega_h} + \|\varepsilon_u(t^n)\|_{\Omega_h} \leq C (\Delta t + h^{\min\{s,k\}}). \quad \square$$

24

25 5. Numerical results

26 In this section, we conduct several numerical experiments to evaluate the performance of the proposed exponential
27 DG framework for both Burgers and Euler equations. In particular, we examine the numerical stability for a wide

⁹ $\rho^0 = 0$.

Table 1

A time-independent manufactured solution for the viscous Burgers equation: a spatial convergence study using $N_e = \{20, 40, 80, 160\}$ elements is conducted with Lax–Friedrich (LF) flux, entropy flux (EF). EXPRB32 scheme with $\Delta t = 5 \times 10^{-5}$ is used as the time integrator.

	h	LF		EF ($\sigma = 3 \times 10^{-4}$)		EF ($\sigma = 0$)	
		Error	Order	Error	Order	Error	Order
$k = 1$	1/20	4.093E-04	–	4.096E-04	–	4.097E-04	–
	1/40	1.223E-04	1.743	1.225E-04	1.741	1.232E-04	1.734
	1/80	4.494E-05	1.445	4.378E-05	1.484	4.620E-05	1.415
	1/160	1.937E-05	1.214	1.562E-05	1.487	2.074E-05	1.155
$k = 2$	1/20	2.630E-06	–	2.632E-06	–	2.634E-06	–
	1/40	3.210E-07	3.034	3.213E-07	3.034	3.222E-07	3.031
	1/80	3.966E-08	3.017	3.952E-08	3.023	3.996E-08	3.011
	1/160	4.916E-09	3.012	4.833E-09	3.032	4.984E-09	3.003
$k = 3$	1/20	1.431E-07	–	1.459E-07	–	1.471E-07	–
	1/40	1.709E-08	3.066	1.742E-08	3.066	1.819E-08	3.015
	1/80	2.003E-09	3.093	1.876E-09	3.215	2.268E-09	3.003
	1/160	2.251E-10	3.154	1.441E-10	3.703	2.834E-10	3.001
$k = 4$	1/20	5.946E-10	–	5.991E-10	–	6.013E-10	–
	1/40	1.827E-11	5.024	1.837E-11	5.027	1.860E-11	5.015
	1/80	5.626E-13	5.021	5.590E-13	5.039	5.796E-13	5.004
	1/160	1.730E-14	5.023	1.690E-14	5.048	1.810E-14	5.001

range of Courant numbers¹⁰ larger than unity, i.e. $Cr > 1$, the high-order convergence in both space and time, the efficiency, and weak and strong parallel scalability. We measure L^2 error for convergence studies by $\|u - \hat{u}\|_{\Omega_h}$ where \hat{u} is either an exact solution or a reference solution.

5.1. Viscous Burgers equation

5.1.1. An exact time-independent smooth solution

We consider a time-independent manufactured solution with $\kappa = 0.03$ for the Burgers equation

$$u(x, t) = \sin(x^2)x(x - 1)$$

by adding the corresponding source term to (9). We perform a spatial convergence study with both Lax–Friedrich (LF) flux and entropy flux (EF) (we take $\sigma = 0$ and $\sigma = 3 \times 10^{-4}$). In order to prevent temporal discretization error from polluting the spatial one, we employ high-order accurate EXPRB32 scheme¹¹ with $\Delta t = 5 \times 10^{-5}$ and $N_e = \{20, 40, 80, 160\}$ elements. The error is measured at $t = 0.01$ and the results are summarized in Table 1. We observe that entropy flux with no additional stabilization (i.e. $\sigma = 0$) and Lax–Friedrichs flux provide similar results, that is, the convergence order is optimal for even solution orders but sub-optimal for odd ones. This similar behavior when using the central flux for diffusion term has been recorded in the literature (see, e.g. [72], and the references therein) and it is also consistent with our analysis in Section 4 in which we have shown that the spatial convergence is sub-optimal. Entropy flux with small additional stabilization seems to asymptotically deliver convergence rates between $k + 1/2$ and $k + 1$ for all solution orders considered in this case, which is better than what we could prove.

¹⁰ We define Courant numbers $Cr := Cr_a + Cr_d$, where $Cr_a := \frac{c\Delta t}{dx}$ for convection part and $Cr_d := \frac{\kappa\Delta t}{(dx)^2}$ for diffusion part. Here, dx is the minimum distance between two LGL nodes; c is the maximum speed in the system, e.g., $c = |u|$ for Burgers equation and $c = |\mathbf{u} \cdot \mathbf{n}| + a$ for Euler equations.

¹¹ EXPRB32 [71] is the third-order two-stage exponential method given by

$$q^{(2)} = q^n + \Delta t \varphi_1(L\Delta t)R^n,$$

$$q^{n+1} = q^n + \Delta t \varphi_1(L\Delta t)R^n + 2\Delta t \varphi_3(L\Delta t)D_{n,2},$$

where $R(q) = Lq + \mathcal{N}(q)$, $R^n := R(q^n)$ and $D_{n,2} := \mathcal{N}(q^{(2)}) - \mathcal{N}(q^n)$. Here, we choose $L = \frac{\partial R}{\partial q}|_{q^n}$.

Table 2

A smooth solution for the viscous Burgers equation: a spatial convergence study using $N_e = \{20, 40, 80, 160\}$ elements is conducted with Lax–Friedrich (LF) flux and entropy flux (EF), and EXPRB32 scheme with $\Delta t = 5 \times 10^{-5}$ as the time integrator.

	h	LF		$EF(\sigma = 3 \times 10^{-4})$		$EF(\sigma = 0)$	
		Error	Order	Error	Order	Error	Order
$k = 1$	1/20	7.061E-03	–	7.157E-03	–	7.161E-03	–
	1/40	2.080E-03	1.764	2.285E-03	1.647	2.308E-03	1.633
	1/80	6.731E-04	1.627	8.552E-04	1.418	9.186E-04	1.329
	1/160	2.432E-04	1.469	3.070E-04	1.478	4.241E-04	1.115
$k = 2$	1/20	2.511E-04	–	2.540E-04	–	2.541E-04	–
	1/40	2.741E-05	3.196	2.744E-05	3.210	2.744E-05	3.211
	1/80	3.317E-06	3.047	3.317E-06	3.048	3.317E-06	3.048
	1/160	4.112E-07	3.012	4.113E-07	3.012	4.112E-07	3.012
$k = 3$	1/20	2.574E-05	–	2.738E-05	–	2.748E-05	–
	1/40	2.883E-06	3.158	3.243E-06	3.078	3.311E-06	3.053
	1/80	3.414E-07	3.078	3.748E-07	3.113	4.087E-07	3.018
	1/160	4.108E-08	3.055	3.722E-08	3.332	5.091E-08	3.005
$k = 4$	1/20	9.225E-07	–	9.273E-07	–	9.273E-07	–
	1/40	2.529E-08	5.189	2.785E-08	5.057	2.858E-08	5.020
	1/80	7.135E-10	5.147	7.563E-10	5.202	8.445E-10	5.081
	1/160	2.188E-11	5.027	2.190E-11	5.110	2.604E-11	5.019

5.1.2. A smooth solution

We next consider a case with smooth solution generated by the following initial condition,

$$u(x, t = 0) = \sin^3(2\pi x)(1 - x)^{\frac{3}{2}},$$

zero Dirichlet boundary conditions, and $\kappa = 0.03$. The smooth initial profile is spread out due to the viscosity as time goes by.

We conduct a spatial convergence study with both LF and EF fluxes with $N_e = \{20, 40, 80, 160\}$. We again use EXPRB32 for the time integrator with $\Delta t = 5 \times 10^{-5}$. Since there is no exact solution we use RK4 solution with $\Delta t = 5 \times 10^{-7}$, $k = 10$, and $N_e = 160$ as the “ground truth” solution. The error at $t = 0.01$ is used to compute the convergence rate and the results are summarized in Table 2. Similar to the case of the manufactured solution, we observe that the convergence rates for odd solution orders are sub-optimal, but optimal for even solution orders. Again, a little additional stabilization via σ not only facilitates our convergence analysis but also seems to improve the convergence rates.

Before showing temporal convergence rates let us demonstrate the numerical stability of exponential integrators by using very large Courant numbers. For this purpose, it is sufficient to choose EPI2 scheme.¹² We compare EPI2 and RK2 solutions at $t = 1$, both with EF flux, in Fig. 1. For RK2 solution, we take $\Delta t = 10^{-4}$ ($Cr_d = 0.16$) as approximately the maximal stable timestep size since $\Delta t = 2 \times 10^{-4}$ leads to instability. Unlike RK2, with 1000 times larger timestep size, i.e. $Cr_d = 161.0$, EPI2 still produces a comparable result compared to RK2. Even with 5000 times larger timestep size ($Cr_d = 804.9$), EPI2 solution is still stable though less accurate (see Fig. 1(b) in which we compare the accuracy of EPI2 and RK2 using RK4 with $\Delta t = 5 \times 10^{-6}$ as a reference solution). As for the wallclock time, RK2 takes 8.3 s, whereas EPI2 does 1.6 s with $Cr_d = 161.0$ and 1.3 s with $Cr_d = 804.9$. EPI2 is five to six times faster than RK2 in this example.

We now compute the temporal convergence rates of two exponential integrators, EPI2 and EXPRB32, using our DG spatial discretization with $k = 4$ and $N_e = 40$. To that end, we take the RK4 solution with $\Delta t = 5 \times 10^{-6}$ as a ground truth. The error is computed at $t = 1$. As can be seen in Table 3, the numerical results with both LF and

¹² EPI2 [48] is the second-order exponential method given by

$$q^{n+1} = q^n + \Delta t \varphi_1(L\Delta t)R^n$$

where $L = \frac{\partial R}{\partial q} \Big|_{q^n}$.

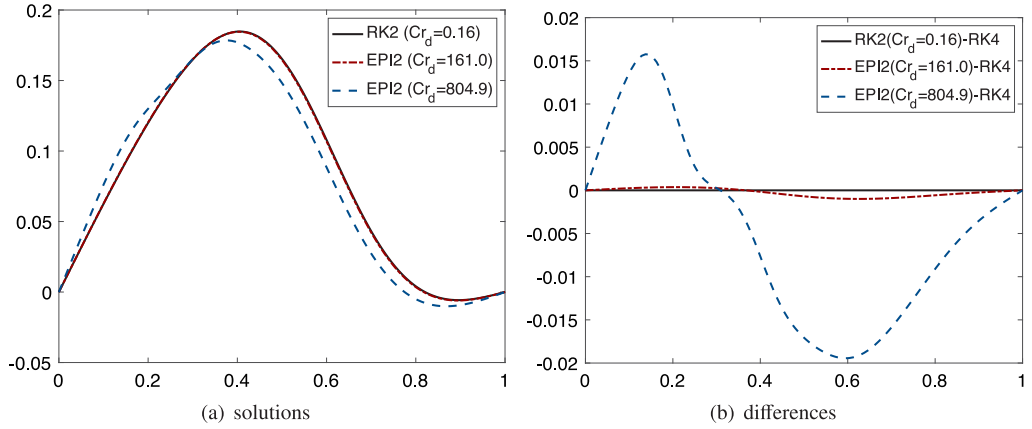


Fig. 1. Accuracy comparisons between EPI2 and RK2 using Burgers equation with smooth solutions at $t = 1$ with $k = 4$ and $N_e = 40$: Fig. 1(a) shows RK2 with $Cr_d = 0.16$ (black), EPI2 with $Cr_d = 161.0$ (red-dashed), and EPI2 with $Cr_d = 804.9$ (blue-dashed). Fig. 1(b) plots their differences with RK4 solution with $dt = 5 \times 10^{-6}$. (For interpretation of the references to color in this figure legend, the reader is referred to the web version of this article.)

Table 3

Temporal convergence rates for EPI2 and EXPRB32 for a smooth solution of the viscous Burgers equation by computing the error at $t = 1$ using RK4 solution with $\Delta t = 5 \times 10^{-6}$ as the reference solution. Spatial discretization is carried out using our DG approach with $k = 4$ and $N_e = 40$. We observe second- and third-order convergence rates for EPI2 and EXPRB32, respectively.

Flux	Δt	Cr_d	EPI2		EXPRB32	
			Error	Order	Error	Order
LF	0.50	804.9	1.171E-02	–	5.272E-03	–
	0.25	402.5	3.303E-03	1.827	1.077E-03	2.292
	0.10	161.0	5.411E-04	1.974	9.575E-05	2.641
	0.05	80.5	1.312E-04	2.044	1.300E-05	2.881
	0.01	16.1	4.943E-06	2.037	1.042E-07	2.999
EF($\sigma = 3 \times 10^{-4}$)	0.50	804.9	1.171E-02	–	5.272E-03	–
	0.25	402.5	3.303E-03	1.827	1.077E-03	2.292
	0.10	161.0	5.411E-04	1.974	9.575E-05	2.641
	0.05	80.5	1.312E-04	2.044	1.300E-05	2.881
	0.01	16.1	4.943E-06	2.037	1.042E-07	2.999
EF($\sigma = 0$)	0.50	804.9	1.171E-02	–	5.272E-03	–
	0.25	402.5	3.303E-03	1.827	1.077E-03	2.292
	0.10	161.0	5.411E-04	1.974	9.575E-05	2.641
	0.05	80.5	1.312E-04	2.044	1.300E-05	2.881
	0.01	16.1	4.943E-06	2.037	1.043E-07	2.988

EF fluxes show second- and third-order convergence rates for EPI2 and EXPRB32, respectively. We observe that the difference in the solutions of LF and EF are negligibly small (on the order of $\mathcal{O}(10^{-9})$). This, we believe, is due to the diffusion-dominated regime, for which different numerical fluxes for the nonlinear convection term do not make (much) difference on the solution.

5.1.3. A solution with steep gradient

We next consider a solution with steep gradient, namely, a stationary shock that evolves in time from the following initial condition

$$u(x, t = 0) = \sin(2\pi x), \quad \text{for } x \in [0, 1],$$

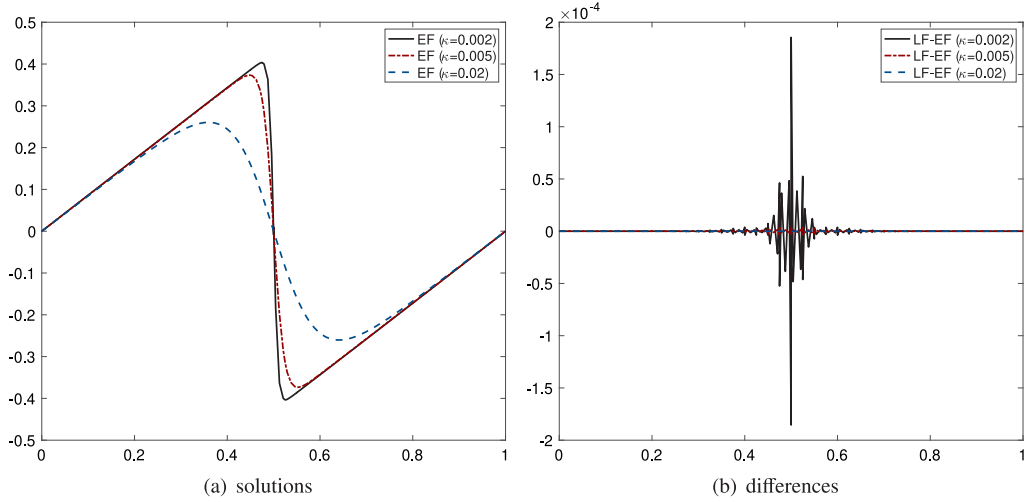


Fig. 2. Burgers equation with a steep gradient solution with EPI2 time integrator, $k = 4$, and $N_e = 40$ at $t = 1$: (a) the snapshots with $\kappa = \{0.02, 0.005, 0.0002\}$ and (b) the solution differences between LF and EF fluxes.

1 and homogeneous boundary conditions. We perform the simulation for $t \in [0, 1]$ with $k = 4$ and $N_e = 40$. As
 2 time goes on, a sharp interface is progressively formed at $x = 0.5$. In this convection-dominated example, EF
 3 flux with a uniform bound of σ leads to an unstable solution, whereas LF flux still produces a stable solution.
 4 This may be related to the growth of aliasing errors arising from the sharp gradient, or insufficient artificial
 5 diffusion between the elements due to the lack of upwinding of the uniform value of σ . Inspired by LF flux,
 6 we set $\sigma = \kappa/100 + h \max(|u^\pm|)$ for EF flux in this example. Fig. 2 are the EPI2 solution snapshots at $t = 1$ with
 7 $dt = 0.01$ and $\kappa \in \{0.02, 0.005, 0.002\}$. By decreasing κ , the shock solutions with EF flux become stiffer, and the
 8 difference of EPI2 solutions between LF flux and EF flux increases up to $\mathcal{O}(10^{-4})$.

9 With $\kappa = 0.002$, we now perform spatial and temporal convergence studies. For spatial convergence study, we
 10 use nested meshes with $N_e = \{40, 80, 160\}$ ¹³ and the EXPRB32 integrator with $\Delta t = 5 \times 10^{-5}$. RK4 solution (with
 11 LF flux, $\Delta t = 5 \times 10^{-7}$, $k = 10$, and $N_e = 160$) is used as the “ground truth” solution for measuring the L^2 error
 12 at $t = 1$. We observe $k + \frac{1}{2}$ rate of convergence for both LF and EF fluxes in Table 4.

13 For temporal convergence study, we consider the DG discretization with $k = 4$, and $N_e = 160$. We take the RK4
 14 solution (with LF flux, $\Delta t = 5 \times 10^{-7}$, $k = 10$, and $N_e = 160$) as a reference solution to measure the L^2 error at
 15 $t = 1$. In Table 5, we observe second- and third-order convergence rates for EPI2 and EXPRB32, respectively.

16 Considering the simplicity and upwinding nature of Lax–Friedrich flux, we use Lax–Friedrich flux for Euler
 17 equations (which are hyperbolic) in the following examples.

18 5.2. Euler equations: Isentropic vortex translation

We consider the isentropic vortex example in [73], where a small vortex perturbation is added to the uniform
 mean flow and translated without changing its shape. The superposed flow is given as

$$u = u_\infty - \frac{\lambda}{2\pi} \tilde{y} e^{\alpha(1-r^2)/2}, \quad v = v_\infty + \frac{\lambda}{2\pi} \tilde{x} e^{\alpha(1-r^2)/2},$$

$$T = T_\infty - \left(\frac{1}{2\alpha c_p} \right) \left(\frac{\lambda}{2\pi} \right)^2 e^{\alpha(1-r^2)},$$

19 where $r = \|\mathbf{x} - \mathbf{x}_c - \mathbf{u}_\infty t\|$, $\tilde{x} = x - x_c - u_\infty t$, $\tilde{y} = y - y_c - v_\infty t$, $\mathbf{u}_\infty = (u_\infty, v_\infty)$, and $\mathbf{x}_c = (5, 0)$.
 20 Here, c_p is the specific heat ratio at constant pressure and λ the vortex strength. The mean flow is set to be
 21 $(u_\infty, v_\infty, \rho_\infty, T_\infty, p_\infty) = (0.2, 0, 1, 1, 1)$. We take $\alpha = 2$, $\gamma = 1.4$, $\lambda = 0.05$ and $c_p = \frac{\gamma}{\gamma-1}$. The exact solution is

¹³ All the meshes are chosen to align with the sharp interface at $x = 0.5$.

Table 4

A shock solution to the viscous Burgers equation with a spatial convergence study using $N_e = \{40, 80, 160\}$ elements is conducted with Lax–Friedrich (LF) flux and entropy flux (EF), and EXPRB32 scheme with $\Delta t = 5 \times 10^{-5}$ as the time integrator. We take the RK4 solution (with $\Delta t = 5 \times 10^{-7}$, $k = 10$, and $N_e = 160$) as a reference solution to measure the L^2 error at $t = 1$.

	h	LF		EF	
		Error	Order	Error	Order
$k = 1$	1/40	1.295E–02	–	1.353E–02	–
	1/80	5.558E–03	1.221	5.577E–03	1.279
	1/160	2.001E–03	1.474	1.964E–03	1.506
$k = 2$	1/40	4.223E–03	–	4.229E–03	–
	1/80	6.722E–04	2.651	6.712E–04	2.656
	1/160	9.852E–05	2.770	9.616E–05	2.803
$k = 3$	1/40	9.976E–04	–	9.969E–04	–
	1/80	1.435E–04	2.797	1.449E–04	2.782
	1/160	1.224E–05	3.551	1.219E–05	3.571
$k = 4$	1/40	3.606E–04	–	3.577E–04	–
	1/80	2.728E–05	3.724	2.706E–05	3.725
	1/160	8.084E–07	5.077	7.432E–07	5.186

Table 5

Temporal convergence study of EPI2 and EXPRB32 for a shock solution to the viscous Burgers equation: we take the RK4 solution (with LF flux, $\Delta t = 5 \times 10^{-7}$, $k = 10$, and $N_e = 160$) as a reference solution, and measure the L^2 error at $t = 1$. Spatial discretization is carried out using our DG approach with $k = 4$ and $N_e = 160$. We observe second- and third-order convergence rates for EPI2 and EXPRB32, respectively.

Flux	Δt	Cr	EPI2		EXPRB32	
			Error	Order	Error	Order
LF	0.25	559.1	2.276E–02	–	8.424E–03	–
	0.10	213.3	3.706E–03	1.981	5.711E–04	2.937
	0.05	105.5	8.784E–04	2.077	6.440E–05	3.149
	0.02	42.0	1.327E–04	2.063	3.755E–06	3.102
EF	0.25	559.1	2.276E–02	–	8.424E–03	–
	0.10	213.3	3.706E–03	1.981	5.711E–04	2.937
	0.05	105.5	8.784E–04	2.077	6.440E–05	3.149
	0.02	42.0	1.327E–04	2.063	3.745E–06	3.105

generated from the isentropic relation.¹⁴ The domain is $\Omega = (0, 10) \times (-5, 5)$ and periodic boundary conditions are applied to all directions. For a three-dimensional simulation, we take the zero vertical velocity, $w = 0$, and extrude the 2D domain vertically from 0 to 1 to obtain $\Omega = (0, 10) \times (-5, 5) \times (0, 1)$.

5.2.1. Stability of exponential integrators

We perform the simulation for $t \in [0, 15]$ with $k = 12$ and $N_e = 256$ in Fig. 3. Compared to the stable EPI2 solution with $\Delta t = 0.5$ (i.e. $Cr = 42.75$) in Fig. 3(a), the EPI2 solution with $\Delta t = 1$ ($Cr = 85.56$) in Fig. 3(b) is oscillatory (part of the domain away from the vortex). One can reduce the oscillation while keeping large Courant

$$\frac{\rho}{\rho_\infty} = \left(\frac{T}{T_\infty} \right)^{\frac{1}{\gamma-1}} = \left(\frac{p}{p_\infty} \right)^{\frac{1}{\gamma}}$$

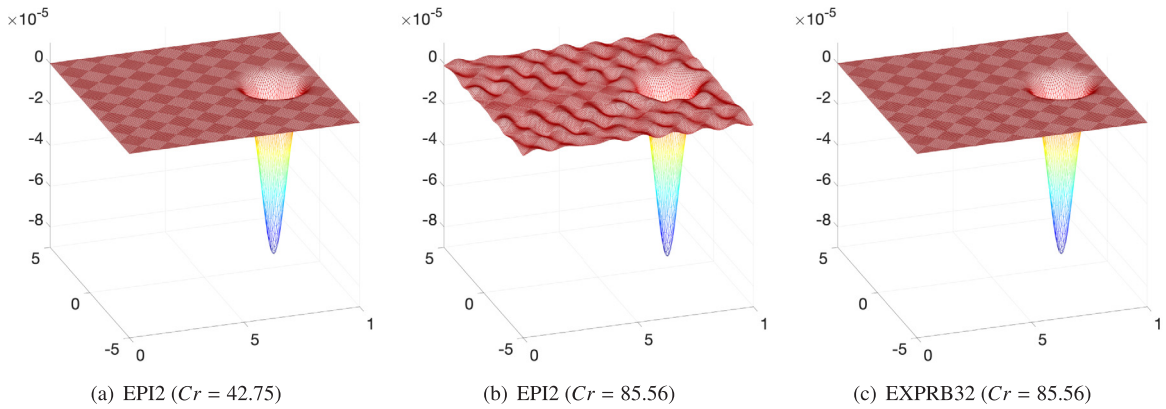


Fig. 3. Translating isentropic vortex example for the two-dimensional Euler equations at $t = 15$: numerical solution using EPI2 with $Cr = 42.75$ is in Fig. 3(a), using EPI2 with $Cr = 85.56$ in Fig. 3(b), and using EXPRB32 with $Cr = 85.56$ in Fig. 3(c).

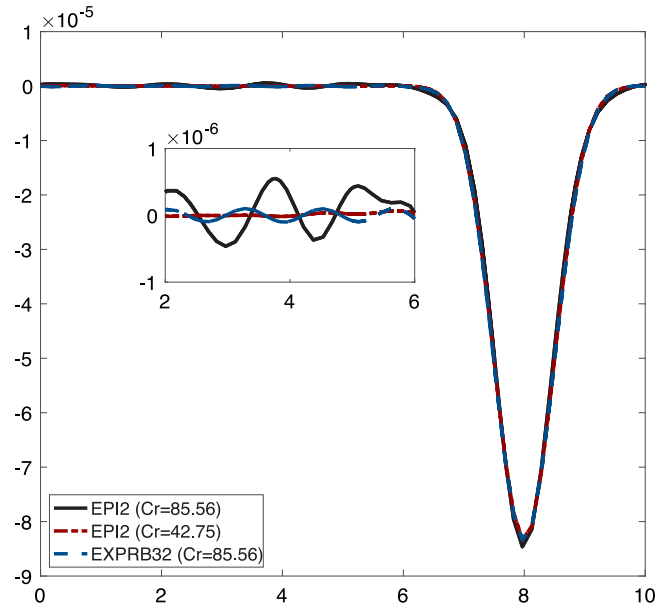


Fig. 4. Translating isentropic vortex example for the two-dimension (black is for EPI2 with $Cr = 85.56$, red-dashed for EPI2 with $Cr = 42.75$, and blue-dashed for EXPRB32 with $Cr = 85.56$) Euler equations at $t = 15$: a slice along $y = 0$ for all sub-figures in Fig. 3. (For interpretation of the references to color in this figure legend, the reader is referred to the web version of this article.)

1 number by employing a more accurate, e.g. higher-order, time integrator.¹⁵ To demonstrate this point we show the
 2 third-order EXPRB32 solution with $\Delta t = 1$ ($Cr = 85.56$) in Fig. 3(c) for which oscillations are not visible in the
 3 same scale. A closer look, see Fig. 4, in which we plot a slice along $y = 0$ for all sub-figures in Fig. 3, shows
 4 that the EXPRB32 solution with ($Cr = 85.56$) does reduce oscillations. This is not surprising: *though exponential*
 5 *integrators are inherently implicit, large timestep size must be chosen with care in order to avoid adverse affect on*
 6 *the accuracy.*

¹⁵ Since high-order methods require more nonlinear evaluations, the evolution of the solution can be captured more accurately than the low-order methods. For example, EPI2 needs one nonlinear evaluation at t^n , whereas EXPRB32 uses two nonlinear evaluations at t^n and t^{n+1} .

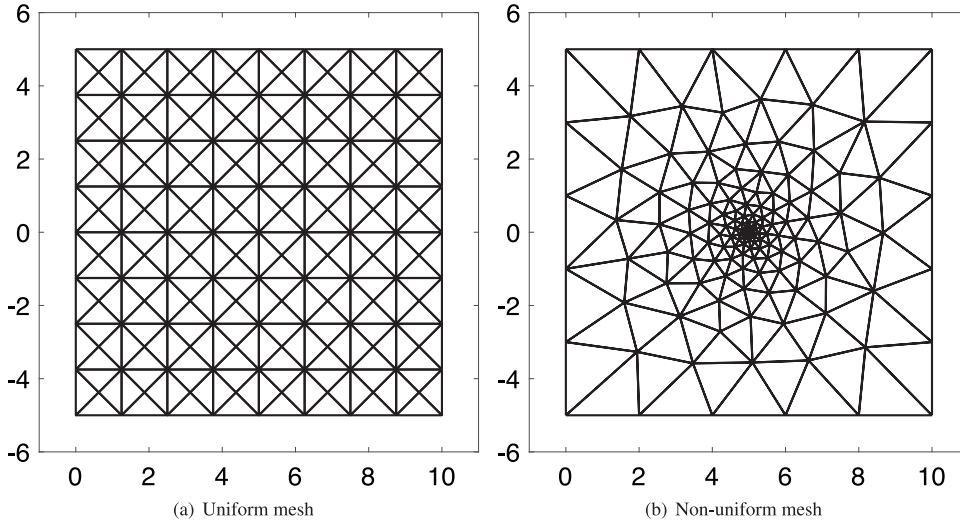


Fig. 5. (a) A uniform mesh with $N_e = 256$ elements, and (b) a non-uniform meshes with $N_e = 250$ elements.

5.2.2. Accuracy and efficient comparison among exponential integrators

In this section, we take the second, the third, and the fourth-order exponential integrators: EPI2, EXPRB32, and EXPRB42,¹⁶ respectively, and compare their relative accuracy and efficiency. Time convergence studies are conducted on a uniform mesh and a non-uniform mesh in Fig. 5.

We start with a very high-order accurate discretization in space with $k = 16$ for the uniform mesh so that the spatial error (around 10^{-13}) does not pollute the temporal one. Fig. 6(a) presents the L^2 -error for the density ρ over a wide range of timestep sizes. Note that the numbers on the top of the figure is the corresponding Courant number for the timestep size displayed on the x -axis. As can be seen, EPI2, EXPRB32, and EXPRB42 achieve expected convergence rate of 2, 3, and 4, respectively. Beyond 10^{-13} the error is dominated by spatial discretization error, which explains why the error for the last two points (the two smallest timestep size cases) of the EXPRB42 error curve plateaus.

5.2.3. Accuracy and efficient comparison between exponential and IMEX integrators

We now compare exponential methods with IMEX (implicit–explicit) time integrators. For IMEX integrators, we integrate the linearized operator L implicitly and the nonlinear operator \mathcal{N} explicitly. We consider the second-order ARS232 [21] and the third-order ARS443 [21] IMEX schemes. The L^2 -error for ρ corresponding to these IMEX methods on the uniform mesh are summarized in Fig. 6. As can be seen in Fig. 6(a), for a given timestep size EXPRB32 is (an order of magnitude) more accurate than ARS443 while EPI2 is (about half order of magnitude) less accurate than ARS232. Efficiency comparison in Fig. 6(b) shows that, for a given level of accuracy, exponential integrators EXPRB32 and EPI2 are much (from two to ten times) more efficient than the IMEX counterparts ARS232 and ARS443. Though both EXPRB32 and EXPRB42 require two matrix exponential evaluations, and hence having similar wallclock, EXPRB42, due to its high-order accuracy, is more efficient than EXPRB32.

5.2.4. Accuracy and efficient comparison between exponential and RK integrators

We next compare exponential methods with explicit RK (Runge–Kutta) time integrators. We consider second-order RK2, third-order RK3, and fourth-order RK4 methods. Fig. 6(a) shows that RK2 solution converges to the

¹⁶ EXPRB42 [74] is the fourth-order two-stage method,

$$q^{(2)} = q^n + \frac{3}{4}\Delta t\varphi_1\left(\frac{3}{4}L\Delta t\right)R^n,$$

$$q^{n+1} = q^n + \Delta t\varphi_1(L\Delta t)R^n + \frac{32}{9}\Delta t\varphi_3(L\Delta t)D_{n,2},$$

where $R(q) = Lq + \mathcal{N}(q)$, $R^n := R(q^n)$ and $D_{n,2} := \mathcal{N}(q^{(2)}) - \mathcal{N}(q^n)$.

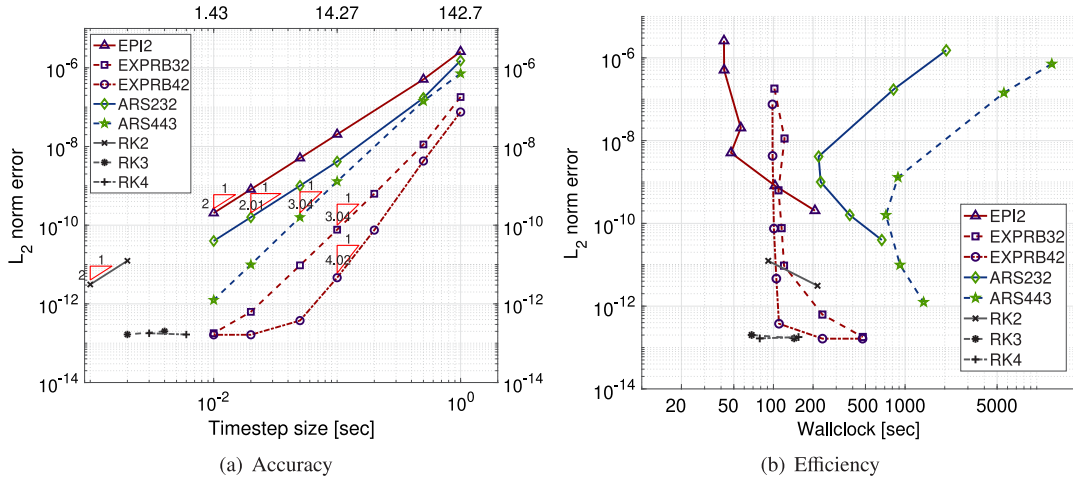


Fig. 6. Accuracy and efficiency of exponential, IMEX, and RK integrators for the isentropic vortex translation in two dimensions on a uniform mesh with $N_e = 256$ and $k = 16$.

1 true solution with the second-order accuracy, while RK3 and RK4 solutions immediately saturate at the error level
 2 of $\mathcal{O}(10^{-13})$ as the temporal error is smaller than the spatial one. Note that the right most point for each of RK
 3 method corresponds to (approximately) the largest stable timestep size. Exponential methods, again due to their
 4 implicit nature, does not have time stepsize restriction. As expected Fig. 6(b) shows that with a same accuracy,
 5 exponential integrators are less efficient than their same order RK counterparts since the formers require matrix
 6 exponential evaluations. Times taken by high-order exponential integrators become comparable to low-order RK
 7 counterparts. This should not understood as a disadvantage. On the contrary, the main advantage of EI is on stiff
 8 problems or problem requires large time stepsizes (with CFL number greater than 1) for which explicit RK methods
 9 fail. The example shows that the cost of exponential methods are similar to stable explicit RK methods while stably
 10 providing solutions with time stepsizes orders of magnitude larger than the maximal stable time stepsizes for explicit
 11 RK methods.

12 On the non-uniform mesh, we set the center of the vortex to be $\mathbf{x}_c = (0, 0)$ at $t = 0$ so that the initial vortex is
 13 defined on a coarse region. This means that more spatial discretization error is introduced than that on the uniform
 14 mesh. In Fig. 7(a), the saturated error level of $\mathcal{O}(10^{-11})$ is higher than the counterpart on the uniform mesh. All RK
 15 solutions immediately reach to the saturated error level of $\mathcal{O}(10^{-11})$. In Fig. 7(b) and Table 6, RK4 is faster than
 16 RK2 and RK3. Compared to RK4, Exponential DG methods show slightly better performance at the error level of
 17 $\mathcal{O}(10^{-11})$. For example, EPI2 with $Cr = 7.49$ is 1.5 times faster than RK4.

18 When we lower the solution order from $k = 16$ to $k = 8$, we see the computational gain of Exponential DG
 19 methods in Table 7. All the numerical solutions saturate at $\mathcal{O}(10^{-6})$ error level. The wallclock times of RK2, RK3,
 20 and RK4 are 155.8, 150.0, and 101.9. EPI2 is three times faster than RK2 and RK3, and two times faster than RK4.
 21 EXPRB32 and EXPRB42 slightly better perform RK4.

22 To demonstrate the high-order convergence in space, we perform the spatial convergence test. We use a sequence
 23 of nested meshes with $N_e = (256, 1024, 4096, 16384)$ for $k = (1, 2, 3, 4)$ and measure the errors at $t = 1$. As can
 24 be seen in Table 8, the convergence rate of $(k + \frac{1}{2})$ is observed as refining the meshes.

25 5.2.5. Performance of exponential DG on parallel computers

26 Now we study the parallel performance, namely weak and strong scalings, of Exponential DG methods for three-
 27 dimensional Euler equations. For this purpose, we choose the EPI2 integrator. Parallel simulations are conducted
 28 on Stampede2 at the Texas Advanced Computing Center (TACC) using Skylake (SKX) nodes. Each node of SKX
 29 consists of 48 cores of Intel Xeon Platinum 8160 2.1 GHz processors and 192 GB DDR4 RAM. The interconnect
 30 is a 100 GB/s Intel Omni-Path (OPA) network with a fat-tree topology.

31 We begin with strong scaling in which the problem size is fixed while the number of cores increases. Table 9
 32 compares the efficiencies of two different timestep sizes: $\Delta t = 0.125$ and $\Delta t = 0.25$ on the mesh with $N_e = 51200$

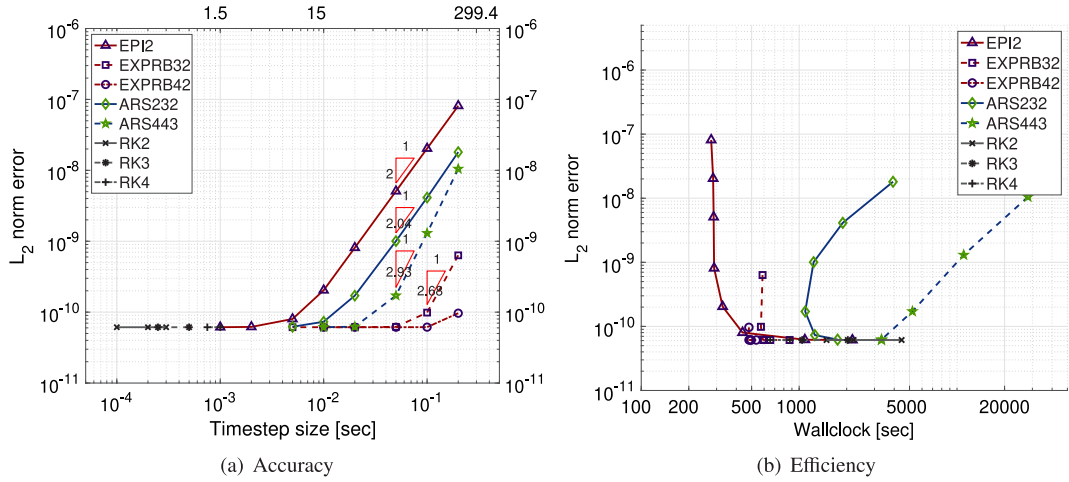


Fig. 7. Isentropic vortex translation in two dimensions: time convergence study for (a) accuracy and (b) efficiency on non-uniform mesh. The computational domain is discretized with $N_e = 250$ and $k = 16$.

(elements) and $k = 6$ (solution order). For either of the timestep sizes, the corresponding run with 32 cores and 1600 elements per core is served as the based line. As the number of cores increases (i.e. the number of elements per core decreases) communication-computation overlapping is less effective and thus decreasing the efficiency. The efficiency with $\Delta t = 0.125$ is slightly higher than that with $\Delta t = 0.25$ as the latter requires more Krylov iterations than the former: the total number of Krylov iterations N_{Krylov} is 561 for $Cr = 15.49(\Delta t = 0.125)$ and 1024 for $Cr = 32.98(\Delta t = 0.25)$.¹⁷ This implies that the spectrum of the linear operator becomes broad by increasing the timestep size.¹⁸

Next, we conduct a strong scaling test using the exponential DG with EPI2, $Cr = 8.1$ ($\Delta t = 0.03125$), $N_e = 3, 276, 800$ and $k = 4$. We choose the number of processors to be $n_p = \{16, 32, 64, 128, 256, 512, 868\} \times 48$ so that the number of elements per core approximately becomes $\{4267, 2133, 1067, 533, 267, 133, 79\}$, i.e., every time we double the number of processors, the number of elements is halved. The speedup factors¹⁹ for all cases in Fig. 8 show that the exponential DG approach delivers good strong scalability up to 41664 cores—the maximum number of cores in Skylake system in TACC.

For the weak scaling test, we assign the same amount of work to each processor (by refining the mesh) while increasing the number of processors. Our exponential DG approach uses EPI2, $N_e = \{1, 8, 64, 512, 4096\} \times 100$, and $k = 8$. The number of processors is chosen in the set $\{4, 32, 256, 2048, 16384\}$ so that the number of elements per core is 25 (i.e. 18,225 degrees-of-freedom). We have tabulated the weak scaling results in Table 10, in which each row block shows, for a fixed Courant number, the number of processors, the timestep sizes, the final times, the wallclock times taken, and the number of Krylov iterations. For each fixed Courant number, good weak scalings can be seen through the wallclock times (and N_{Krylov}) that do not vary much as the number of processors (and thus the problem size) increases. To see this visually, we plot the average time-per-timestep against the number of degrees-of-freedom in Fig. 9: almost plateau curve for each Courant number indicates favorable weak scaling can be obtained by the Exponential DG method. As can also be observed, the number of Krylov iterations N_{Krylov} , and hence the wallclock time, scales linearly with the Courant number.

How does the weak scaling behaves if we fix timestep size Δt instead of Courant number Cr ? In this case, refining the mesh (in order to keep the number of elements per core the same) adds geometrically-induced stiffness to the system, and thus making the total number of Krylov iterations to increase. This is verified in Table 11, which

¹⁷ We observe $N_{Krylov} = 556$ for $Cr = 7.75(\Delta t = 0.0625)$. The total number of Krylov iterations is proportional to Courant number above a certain Courant number. In Table 11, N_{Krylov} is about 40 for $Cr \leq 2.8$. However, for $Cr > 2.8$, doubling Courant number tends to double N_{Krylov} .

¹⁸ Note that the input argument of φ -function is $\Delta t L$.

¹⁹ Speedup is defined as $\frac{T_s}{T_p}$ with T_s serial wallclock time and T_p parallel wallclock time.

Table 6

Isentropic vortex translation in two dimensions: time convergence study on a nonuniform mesh. The computational domain is discretized with $N_e = 256$ and $k = 16$. The error is measured at $T = 1$.

$k = 16$	Cr	ρ		$\rho \mathbf{u}$		ρE		wc [s]
		Error	Order	Error	Order	Error	Order	
RK2	0.45	6.126E-11	-	1.378E-10	-	3.539E-11	-	1491.5
	0.30	6.127E-11	-0.000	1.368E-10	0.018	3.533E-11	0.004	2213.5
	0.15	6.127E-11	0.000	1.366E-10	0.002	3.531E-11	0.001	4457.2
RK3	0.75	6.127E-11	-	1.366E-10	-	3.530E-11	-	1044.9
	0.37	6.127E-11	0.000	1.366E-10	0.000	3.530E-11	0.000	2033.4
RK4	1.50	6.127E-11	-	1.366E-10	-	3.530E-11	-	655.7
	1.12	6.127E-11	0.000	1.366E-10	0.000	3.530E-11	0.000	873.2
EPI2	299.42	8.115E-08	-	9.834E-08	-	2.858E-07	-	277.3
	149.71	2.031E-08	1.998	2.437E-08	2.013	7.153E-08	1.998	285.3
	74.85	5.079E-09	2.000	6.080E-09	2.003	1.788E-08	2.000	287.4
	29.94	8.093E-10	2.004	1.068E-09	1.898	2.840E-09	2.008	289.3
	14.97	2.035E-10	1.992	7.288E-10	0.551	6.848E-10	2.052	327.7
	7.49	8.002E-11	1.347	1.495E-10	2.285	1.823E-10	1.909	438.2
	2.99	6.188E-11	0.281	1.369E-10	0.096	4.527E-11	1.520	1086.7
	1.50	6.132E-11	0.013	1.366E-10	0.003	3.596E-11	0.332	2174.3
EXPRB32	299.42	6.324E-10	-	9.584E-10	-	2.218E-09	-	586.5
	149.71	9.847E-11	2.683	1.865E-10	2.361	2.733E-10	3.021	572.8
	74.85	6.206E-11	0.666	2.220E-10	-0.251	5.044E-11	2.438	588.4
	29.94	6.129E-11	0.014	4.297E-10	-0.721	4.666E-11	0.085	599.2
	14.97	6.133E-11	-0.001	8.731E-10	-1.023	7.249E-11	-0.636	656.4
	7.49	6.127E-11	0.001	1.366E-10	2.676	3.530E-11	1.038	870.0
EXPRB42	299.42	9.660E-11	-	1.735E-10	-	2.707E-10	-	480.6
	149.71	6.142E-11	0.653	1.505E-10	0.205	3.940E-11	2.780	481.6
	74.85	6.127E-11	0.004	2.662E-10	-0.823	3.946E-11	-0.002	496.9
	29.94	6.128E-11	-0.000	4.534E-10	-0.581	4.786E-11	-0.211	491.3
	14.97	6.133E-11	-0.001	9.018E-10	-0.992	7.430E-11	-0.635	534.8
ARS232	299.42	1.806E-08	-	1.920E-06	-	1.503E-07	-	3931.8
	149.71	4.127E-09	2.130	4.803E-07	1.999	3.718E-08	2.015	1889.8
	74.85	1.005E-09	2.038	1.201E-07	2.000	9.266E-09	2.005	1234.8
	29.94	1.707E-10	1.935	1.922E-08	2.000	1.481E-09	2.001	1092.3
	14.97	7.321E-11	1.221	4.806E-09	2.000	3.707E-10	1.998	1256.3
	7.49	6.214E-11	0.237	1.209E-09	1.991	9.790E-11	1.921	1751.2
ARS443	299.42	1.049E-08	-	1.183E-07	-	3.750E-08	-	28140.8
	149.71	1.302E-09	3.010	1.484E-08	2.995	4.702E-09	2.996	11017.5
	74.85	1.714E-10	2.925	1.863E-09	2.994	5.787E-10	3.022	5219.5
	29.94	6.235E-11	1.104	1.812E-10	2.543	5.088E-11	2.653	3327.1
	14.97	6.131E-11	0.024	1.374E-10	0.399	3.562E-11	0.514	3319.0

1 shows linear growth in the total number of Krylov iterations as the mesh is refined for $Cr > 2.8$. As shown in
 2 [Fig. 10](#), the increase in number of Krylov iterations induces the growth in wallclock time.

3 5.3. Euler equations: Kelvin–Helmholtz instability

4 Kelvin–Helmholtz instability (KHI) is an important mechanism in the development of turbulence. KHI occurs
 5 when two fluids meet across their interface with different densities and tangential velocities. As time goes by, small
 6 disturbances at the interface grow exponentially, and the interface rolls up into KH rotors [75–77]. The computational
 7 domain is $\Omega = (-5, 5) \times (0, 5)$. We apply periodic boundary condition to the lateral direction, whereas no-slip
 8 boundary condition to the top and the bottom walls.

Table 7

Isentropic vortex translation in two dimensions: time convergence study on a nonuniform mesh. The computational domain is discretized with $N_e = 256$ and $k = 8$. The error is measured at $t = 1$.

$k = 8$	Cr	ρ		$\rho \mathbf{u}$		ρE		wc [s]
		Error	Order	Error	Order	Error	Order	
RK2	0.63	1.533E-06	-	2.884E-06	-	7.851E-07	-	155.8
	0.33	1.533E-06	0.000	2.884E-06	0.000	7.851E-07	0.000	306.7
RK3	0.81	1.533E-06	-	2.884E-06	-	7.851E-07	-	150.0
	0.41	1.533E-06	0.000	2.884E-06	0.000	7.851E-07	0.000	294.3
RK4	1.36	1.533E-06	-	2.884E-06	-	7.851E-07	-	101.9
	0.90	1.533E-06	0.000	2.884E-06	0.000	7.851E-07	0.000	152.5
	0.45	1.533E-06	0.000	2.884E-06	0.000	7.851E-07	0.000	307.7
EPI2	90.42	1.536E-06	-	2.887E-06	-	8.365E-07	-	45.2
	45.21	1.533E-06	0.003	2.885E-06	0.001	7.907E-07	0.081	49.2
	22.60	1.534E-06	-0.001	2.893E-06	-0.004	7.938E-07	-0.006	52.6
	9.04	1.533E-06	0.001	2.884E-06	0.003	7.849E-07	0.012	59.9
	4.52	1.533E-06	0.000	2.884E-06	0.000	7.851E-07	-0.000	113.3
EXPRB32	90.42	1.533E-06	-	2.884E-06	-	7.862E-07	-	91.4
	45.21	1.533E-06	0.000	2.884E-06	0.000	7.862E-07	0.000	94.9
	22.60	1.533E-06	0.000	2.884E-06	0.000	7.866E-07	-0.001	99.5
	9.04	1.533E-06	0.000	2.884E-06	0.000	7.849E-07	0.002	111.0
	4.52	1.533E-06	0.000	2.884E-06	0.000	7.851E-07	-0.000	221.3
EXPRB42	90.42	1.533E-06	-	2.884E-06	-	7.861E-07	-	77.9
	45.21	1.533E-06	0.000	2.884E-06	0.000	7.859E-07	0.000	75.7
	22.60	1.533E-06	0.000	2.884E-06	0.000	7.870E-07	-0.002	81.4
	9.04	1.533E-06	0.000	2.884E-06	0.000	7.849E-07	0.003	110.9
	4.52	1.533E-06	0.000	2.884E-06	0.000	7.851E-07	-0.000	221.1
ARS232	90.42	1.515E-06	-	3.469E-06	-	7.177E-07	-	343.7
	45.21	1.530E-06	-0.014	2.925E-06	0.246	7.612E-07	-0.085	248.6
	22.60	1.533E-06	-0.003	2.887E-06	0.019	7.803E-07	-0.036	205.9
	9.04	1.533E-06	0.000	2.884E-06	0.001	7.852E-07	-0.007	226.1
	4.52	1.533E-06	0.000	2.884E-06	0.000	7.851E-07	0.000	317.7
ARS443	90.42	1.512E-06	-	2.882E-06	-	6.233E-07	-	1616.1
	45.21	1.526E-06	-0.013	2.881E-06	0.001	6.762E-07	-0.118	1050.9
	22.60	1.531E-06	-0.005	2.883E-06	-0.001	7.490E-07	-0.148	765.3
	9.04	1.533E-06	-0.001	2.884E-06	-0.000	7.816E-07	-0.046	684.7
	4.52	1.533E-06	0.000	2.884E-06	0.000	7.846E-07	-0.006	797.5

The initial conditions are chosen as

$$\rho = 1 + \frac{1}{2} \left(\tanh \left(\frac{y - s_1}{a} \right) - \tanh \left(\frac{y - s_2}{a} \right) \right),$$

$$u = 0.1 + \left(\tanh \left(\frac{y - s_1}{a} \right) - \tanh \left(\frac{y - s_2}{a} \right) - 1 \right),$$

$$v = A \sin(2\pi x) \left(\exp \left(-\frac{(y - s_1)^2}{\sigma^2} \right) + \exp \left(-\frac{(y - s_2)^2}{\sigma^2} \right) \right),$$

$$p = \gamma^{-1},$$

where we take $a = 0.05$, $A = 0.01$, $\sigma = 0.2$, $s_1 = 2$, $s_2 = 3$, and $c_{\max} = 0.1$ and $c_E = 1$ for entropy viscosity.

The numerical simulations are performed with EPI2 and RK4 methods over the uniform mesh with $k = 6$ and $N_e = 722$ for $t \in [0, 100]$. We take $\Delta t = 0.005 =: \Delta t_{RK4}$ for RK4, and $\Delta t = 0.04 (= \Delta t_{RK4} \times 8)$ and $\Delta t = 0.5 (= \Delta t_{RK4} \times 100)$ for EPI2. The temperature fields are plotted at $t = 50$ and $t = 100$ in Fig. 11. The wallclock times of RK4, EPI2 (with $\Delta t = 0.04$) and EPI2 (with $\Delta t = 0.5$) are 8729 s, 3505 s and 2656 s, respectively. EPI2 with $\Delta t = 0.04$ (8 times larger time stepsize) are in good agreement with RK4 but about

Table 8

Spatial convergence for the isentropic vortex translation in two dimensions. We use a sequence of nested meshes with $N_e = \{256, 1024, 4096, 16384\}$ for $k = 1, 2, 3, 4$. We use EXPRB42 scheme with $\Delta t = 0.01$ and measure the errors at $t = 1$.

	h	ρ		$\rho\mathbf{u}$		ρE	
		Error	Order	Error	Order	Error	Order
$k = 1$	1.00	9.942E-04	–	7.389E-03	–	1.595E-03	–
	0.50	7.662E-04	0.376	1.999E-03	1.886	5.181E-04	1.622
	0.25	4.344E-04	0.819	5.312E-04	1.912	2.049E-04	1.338
	0.12	2.312E-04	0.910	1.383E-04	1.941	8.571E-05	1.257
$k = 2$	1.00	2.909E-04	–	7.382E-04	–	4.423E-04	–
	0.50	1.201E-04	1.276	1.418E-04	2.380	4.965E-05	3.155
	0.25	3.235E-05	1.892	1.570E-05	3.175	7.084E-06	2.809
	0.12	5.787E-06	2.483	2.084E-06	2.913	1.257E-06	2.495
$k = 3$	1.00	1.286E-04	–	2.343E-04	–	6.979E-05	–
	0.50	1.972E-05	2.705	1.541E-05	3.926	5.605E-06	3.638
	0.25	2.123E-06	3.215	9.655E-07	3.996	4.450E-07	3.655
	0.12	2.112E-07	3.329	6.849E-08	3.817	4.386E-08	3.343
$k = 4$	1.00	2.686E-05	–	3.180E-05	–	1.311E-05	–
	0.50	2.067E-06	3.700	1.283E-06	4.631	4.381E-07	4.903
	0.25	9.543E-08	4.437	4.294E-08	4.901	1.333E-08	5.039
	0.12	4.540E-09	4.394	1.458E-09	4.880	5.294E-10	4.654

Table 9

Isentropic vortex translation in three dimensions: strong scaling results for EPI2 with $Cr = 16.49$ ($\Delta t = 0.125$) and $Cr = 32.98$ ($\Delta t = 0.25$) are performed with $N_e = 51200$ and $k = 6$ up to $t = 1$.

#cores	N_e/core	$\Delta t = 0.125$		$\Delta t = 0.25$	
		Wallclock [s]	Efficiency	Wallclock [s]	Efficiency
32	1600	2346	100	4151	100
64	800	1199	97.8	2121	97.9
128	400	607.7	96.5	1255	82.7
256	200	306.9	95.6	605.7	85.7
512	100	237.3	61.8	419.1	61.9
1024	50	122.7	59.7	219.1	59.2
2048	25	61.33	59.5	118.0	55.0
4096	12.5	33.72	54.4	63.12	51.4

2.5 times faster. However, EPI2 solution with $\Delta t = 0.5$ is quite deviated from RK4 solution. This is due to the way to approximate the entropy residual.²⁰ Note that in this study, the temporal tendency of the entropy residual is approximated by the first-order Euler method, i.e., $\frac{\partial S}{\partial t} \approx \frac{S^n - S^{n-1}}{\Delta t}$. Thus, using different timestep sizes yields different artificial viscosity. The accuracy of the residual computation can be enhanced by incorporating the second-order approximation such as backward differentiation formula, but this is out of the scope of the paper.

5.4. Euler equations: shock problems

Exponential-DG methods are now tested for shock problems by considering benchmark examples in [78].

5.4.1. Riemann problem: case #4

This example develops four shocks. The initial condition with $\gamma = 1.4$ is defined to be

$$\begin{aligned} \rho = 1.1, u = 0, v = 0, p = 1.1 & \quad x > 0.5, y > 0.5, \\ \rho = 0.5065, u = 0.8939, v = 0, p = 0.35 & \quad x \leq 0.5, y > 0.5, \end{aligned}$$

²⁰ Using high-order exponential integrators does not improve the solution quality unlike the isentropic vortex example in Fig. 3.

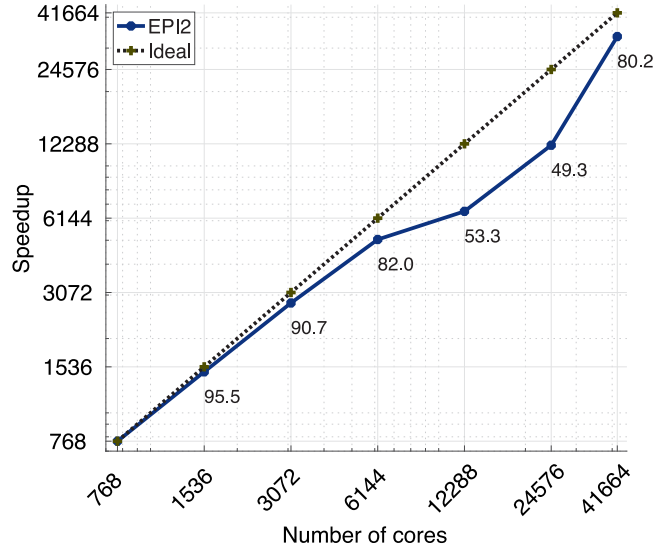


Fig. 8. Isentropic vortex translation in three dimensions: strong scaling study for EPI2 with $Cr = 8.1$ ($\Delta t = 0.03125$). The computational domain is discretized using $N_e = 3, 276, 800$ and $k = 4$. The number of processors used are $n_p = \{16, 32, 64, 128, 256, 512, 868\} \times 48$.

Table 10

Weak scaling study with fixed Courant numbers for the isentropic vortex translation with three dimensional Euler equations. The exponential DG approach consists of EPI2, $N_e = \{1, 8, 64, 512, 4096\} \times 100$, and $k = 8$. Each curve presents the wallclock time per timestep for various number of degrees-of-freedom with a fixed Courant number. The numbers on each of the curves are the number of cores.

Cr	N_e	Δt	Final time	Wallclock [s]	N_{Krylov}
5.59	4	0.2	0.8	15.3	103
	32	0.1	0.4	17.8	90
	256	0.05	0.2	24.4	81
	2048	0.025	0.1	27.8	81
	16384	0.0125	0.05	29.3	82
22.4	4	0.2	0.8	50.4	397
	32	0.1	0.4	89.9	381
	256	0.05	0.2	85.8	355
	2048	0.025	0.1	86.9	348
	16384	0.0125	0.05	93.1	358
55.9	4	0.2	0.8	130.9	1024
	32	0.1	0.4	240.4	1023
	256	0.05	0.2	246.2	1024
	2048	0.025	0.1	248.8	1024
	16384	0.0125	0.05	342.2	1408

$$\rho = 1.1, u = 0.8939, v = 0.8939, p = 1.1$$

$$x \leq 0.5, y \leq 0.5,$$

$$\rho = 0.5065, u = 0, v = 0.8939, p = 0.35$$

$$x > 0.5, y \leq 0.5$$

on $\Omega = (0, 1)^2$. The control parameters of the entropy viscosity are $c_{\max} = 0.1$ and $c_E = 1$.

We conduct the numerical simulation with EPI2 and RK4 methods for $t \in [0, 0.24]$ with $k = 3$ and $N_e = 5000$ in Fig. 12. We take $\Delta t_{RK4} = 0.0004$ for RK4 and $\Delta t = 0.004 (= \Delta t_{RK4} \times 10)$ for EPI2. In general, EPI2 solution is comparable with RK4 counterpart. With 10 times larger time stepsize, EPI2 (taking 324 s) is 4 times faster than RK4 (taking 1366 s).

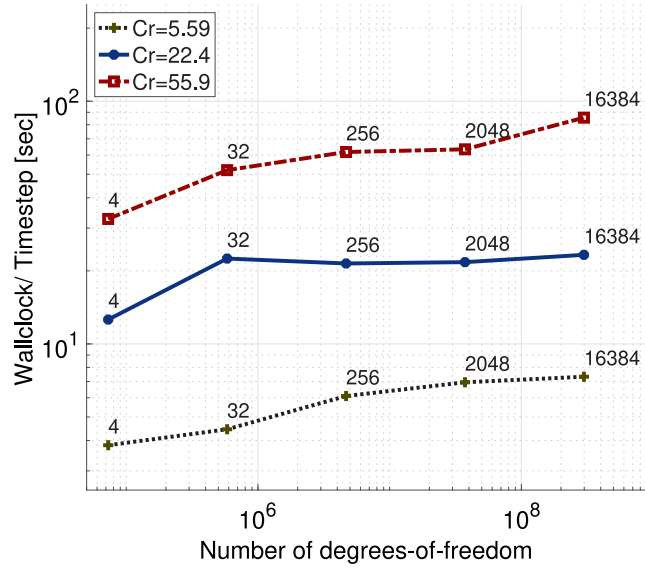


Fig. 9. Weak scaling study with fixed Courant numbers for the isentropic vortex translation with three dimensional Euler equations. The exponential DG approach consists of EPI2, $N_e = \{1, 8, 64, 512, 4096\} \times 100$, and $k = 8$. The number of processors for each N_e is $n_p = \{4, 32, 256, 2048, 16384\}$ so that each processor has 25 elements (18,225 degrees-of-freedom) for all cases.

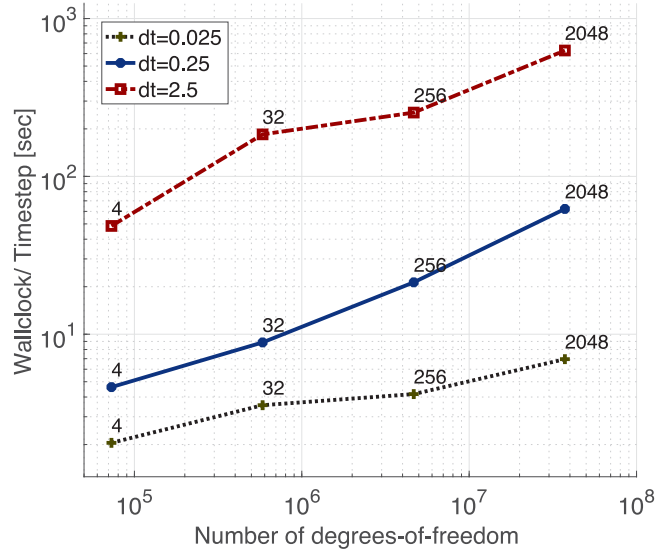


Fig. 10. Weak scaling study with fixed Δt for the isentropic vortex translation with three dimensional Euler equations. The exponential DG approach uses EPI2, $N_e = \{100, 800, 6400, 51200\}$, and $k = 8$. The corresponding number of processors are $n_p = \{4, 32, 256, 2048\}$, respectively, so that each processor has 25 elements for each case.

1 5.4.2. Riemann problem: case #12

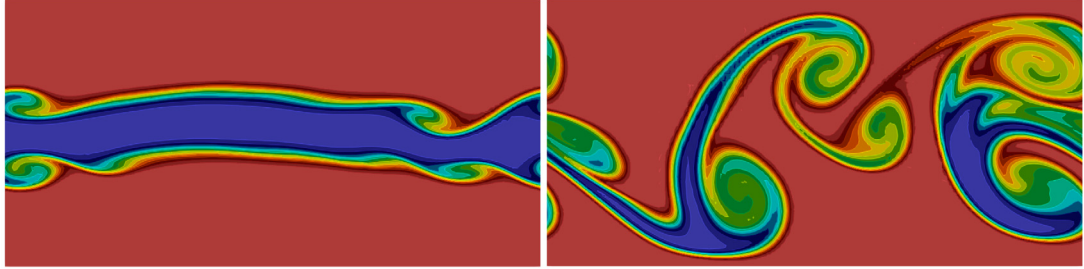
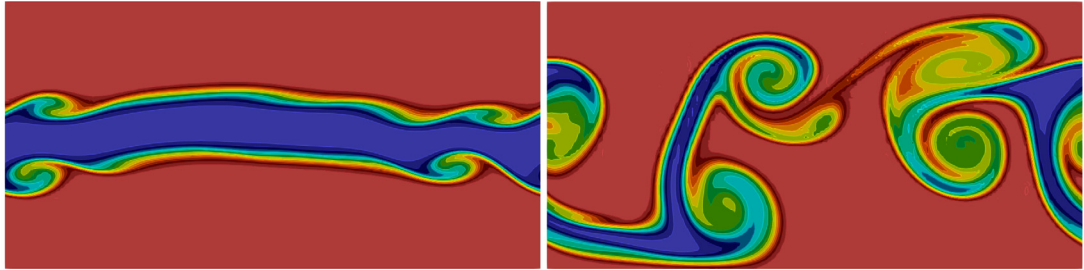
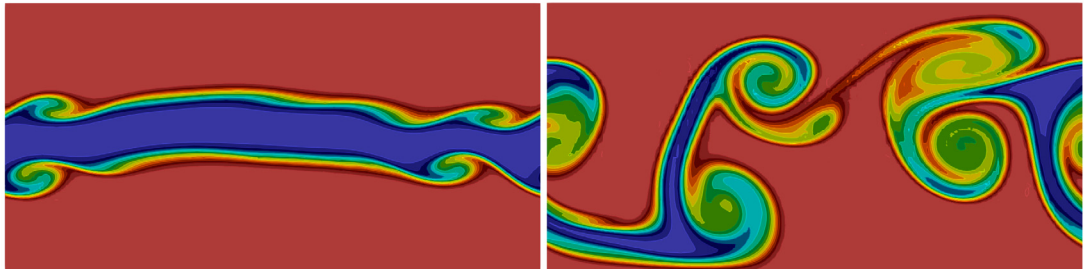
This example develops two contact waves and two shocks. The initial condition with $\gamma = 1.4$ is given as

$$\begin{aligned} \rho &= 0.5313, u = 0, v = 0, p = 0.4 & x > 0.5, y > 0.5, \\ \rho &= 1.0, u = 0.7276, v = 0, p = 1 & x \leq 0.5, y > 0.5, \end{aligned}$$

Table 11

Weak scaling study with fixed dt for the isentropic vortex translation with three dimensional Euler equations. The exponential DG approach uses EPI2, $N_e = \{100, 800, 6400, 51200\}$, and $k = 8$. The corresponding number of processors are $n_p = \{4, 32, 256, 2048\}$, respectively, so that each processor has 25 elements for each case.

Δt	$N_e = 100$		$N_e = 800$		$N_e = 6400$		$N_e = 51200$	
	Cr	N_{Krylov}	Cr	N_{Krylov}	Cr	N_{Krylov}	Cr	N_{Krylov}
0.025	0.7	40	1.4	40	2.8	45	5.6	81
0.25	7.0	128	14.0	233	27.9	448	55.9	1024
2.5	69.8	1536	139.7	3072	279.32	5120	558.7	10112

(a) EPI2 with $\Delta t_{RK4} \times 100$ (b) EPI2 with $\Delta t_{RK4} \times 8$ 

(c) RK4

Fig. 11. Kelvin–Helmholtz instability: evolution of temperature for (a) EPI2 with $dt = 0.5 (= \Delta t_{RK4} \times 100)$, (b) EPI2 with $\Delta t = 0.04 (= \Delta t_{RK4} \times 8)$ and (c) RK4 with $\Delta t = 0.005 (= \Delta t_{RK4})$ at $t = (50, 100)$ on a uniform mesh with $N_e = 722$ and $k = 6$. The temperature ranges from 0.49 to 1.01.

$$\rho = 0.8, u = 0, v = 0, p = 1$$

$$x \leq 0.5, y \leq 0.5,$$

$$\rho = 1.0, u = 0, v = 0.7276, p = 1$$

$$x > 0.5, y \leq 0.5$$

on $\Omega = (0, 1)^2$. The control parameters of the entropy viscosity are $c_{\max} = 0.05$ and $c_E = 0.5$.

We conduct the numerical simulation for $t \in [0, 0.24]$ with $k = 3$ and $N_e = 5000$ in Fig. 13. We take $\Delta t_{RK4} = 0.0004$ for RK4 and $\Delta t = 0.004 (= \Delta t_{RK4} \times 10)$ for EPI2. The wallclock times of RK4 and EPI2

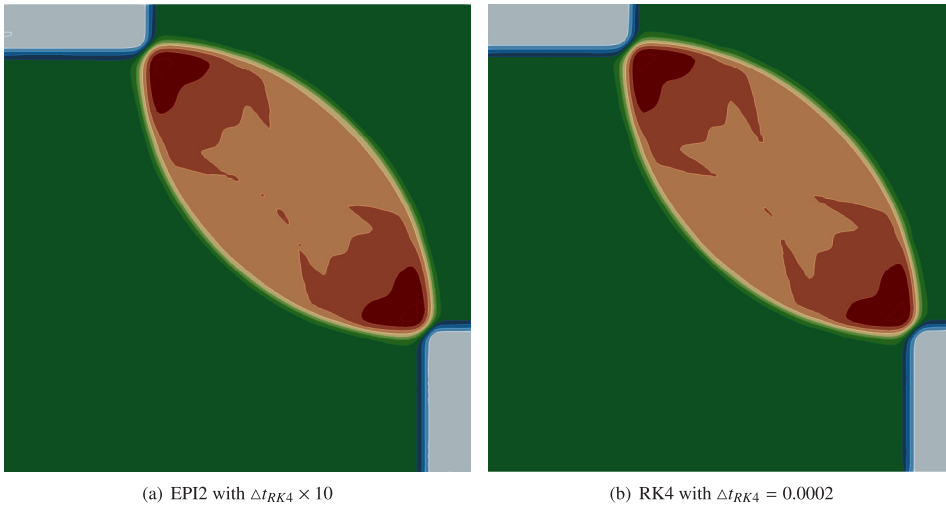


Fig. 12. Riemann problem: case #4: density field of (a) EPI2 with $\Delta t = 0.002 (= \Delta t_{RK4} \times 10)$ and (b) RK4 with $\Delta t_{RK4} = 0.0002$ at $t = 0.25$ on a uniform mesh with $N_e = 5000$ and $k = 3$. The density ranges from 0.5 to 1.9.

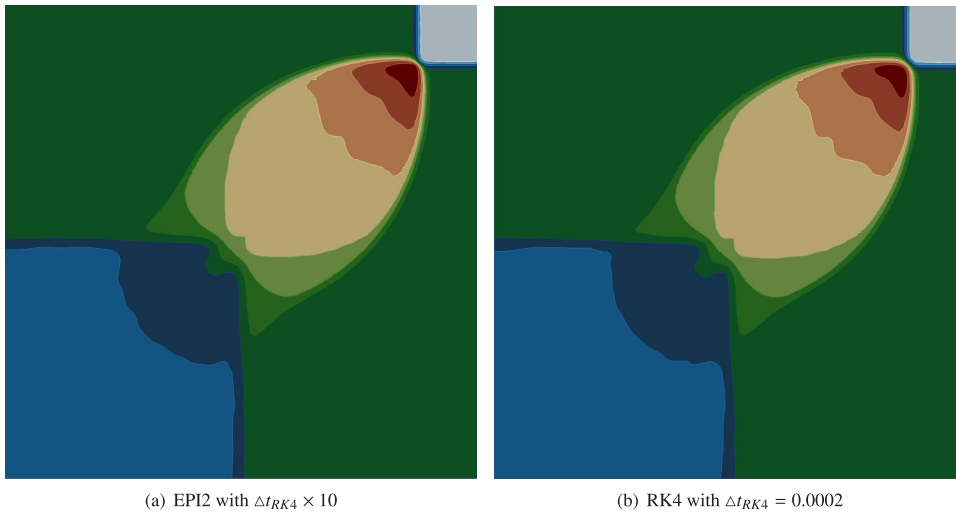


Fig. 13. Riemann problem: case #12: density field of (a) EPI2 with $\Delta t = 0.004 (= \Delta t_{RK4} \times 10)$ and (b) RK4 with $\Delta t_{RK4} = 0.0004$ at $t = 0.24$ on a uniform mesh with $N_e = 5000$ and $k = 3$. The density ranges from 0.5 to 1.7.

1 are 1051.0 s and 327.5 s, respectively. EPI2, with 10 times larger time stepsize, is about 3 times faster than RK4,
 2 and produces the comparable solution to RK4 counterpart.

3 **Fig. 14** shows the viscosity fields of EPI2 and RK4. As mentioned in [62], the viscosity becomes strong in the
 4 shocks, whereas weak in the rest including contact discontinuities. As expected, we also see that the magnitude
 5 of the viscosities for EPI2 and RK4 are different due to the approximation of the entropy residual. Also, the
 6 entropy viscosity method does not completely remove the Gibbs phenomenon associated with high-order spatial
 7 discretization for shock problems. A further study is needed to handle the issue by incorporating several limiters.

8 6. Conclusions

9 In this paper, we have developed an Exponential DG framework. This is done by splitting the governing
 10 differential operator into linear and nonlinear parts to which we apply DG spatial discretization. In particular, we
 11 construct the linear part by linearization aiming to absorb the stiffness in the system. Since the linear–nonlinear
 12 decomposition is done on continuous level, we can avoid taking derivatives of nonsmooth functions possibly

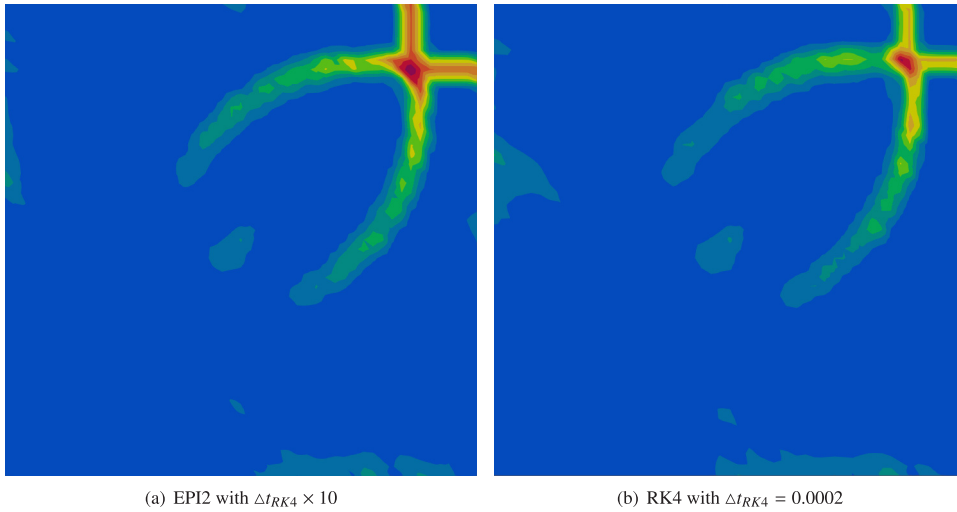


Fig. 14. Riemann problem: case #12: viscosity field of (a) EPI2 with $\Delta t = 0.004 (= \Delta t_{RK4} \times 10)$ and (b) RK4 with $\Delta t_{RK4} = 0.0004$ at $t = 0.24$ on a uniform mesh with $N_e = 5000$ and $k = 3$. The viscosity ranges from 0 to 0.0035.

Table A.12

A time-independent manufactured solution for the viscous Burgers equation: a spatial convergence study using $N_e = \{20, 40, 80, 160\}$ elements is conducted with central (C) flux and local discontinuous Galerkin (LDG) flux for diffusion term. Lax–Friedrich (LF) flux is used for advective term. EXPRB32 scheme with $\Delta t = 5 \times 10^{-5}$ is used as the time integrator.

	h	LF (C)		LF (LDG)	
		Error	Order	Error	Order
$k = 1$	1/20	4.093E-04	–	4.415E-04	–
	1/40	1.223E-04	1.743	1.112E-04	1.990
	1/80	4.494E-05	1.445	2.782E-05	1.998
	1/160	1.937E-05	1.214	6.959E-06	1.999
$k = 2$	1/20	2.630E-06	–	3.586E-06	–
	1/40	3.210E-07	3.034	4.635E-07	2.952
	1/80	3.966E-08	3.017	5.847E-08	2.987
	1/160	4.916E-09	3.012	7.364E-09	2.989
$k = 3$	1/20	1.431E-07	–	6.185E-08	–
	1/40	1.709E-08	3.066	3.713E-09	4.058
	1/80	2.003E-09	3.093	2.270E-10	4.032
	1/160	2.251E-10	3.154	1.404E-11	4.015
$k = 4$	1/20	5.946E-10	–	8.475E-10	–
	1/40	1.827E-11	5.024	2.593E-11	5.030
	1/80	5.626E-13	5.021	8.027E-13	5.014
	1/160	1.730E-14	5.023	2.498E-14	5.006

resulting from both spatial and time discretizations. The resulting semi-discrete system is then integrated with exponential integrators. Our proposed approach aims to (i) circumvent the stringent timestep size arising from explicit integrators; (ii) support high-order accuracy in both space and time; (iii) outperform over IMEX DG methods with no preconditioner; (iv) be comparable to explicit RKDG methods for stiff problems; (v) be scalable in a modern massively parallel computing architecture. We present a detailed stability and convergence analyses for the Burgers equation using the exponential Euler DG scheme.

Numerical results (for Burgers equation and Euler equations) have shown that while explicit RKDG methods suffer from restricted timestep sizes due to numerical stability, Exponential DG framework supports a wide range of Courant numbers. We numerically observe that the proposed methods achieve the high-order temporal and spatial

Table A.13

A smooth solution for the viscous Burgers equation: a spatial convergence study using $N_e = \{20, 40, 80, 160\}$ elements is conducted with central (C) flux and local discontinuous Galerkin (LDG) flux for diffusion term. Lax–Friedrich (LF) flux is used for advective term. EXPRB32 scheme with $\Delta t = 5 \times 10^{-5}$ as the time integrator.

	h	LF (C)		LF (LDG)	
		Error	Order	Error	Order
$k = 1$	1/20	7.061E–03	–	7.234E–03	–
	1/40	2.080E–03	1.764	1.901E–03	1.928
	1/80	6.731E–04	1.627	4.928E–04	1.948
	1/160	2.432E–04	1.469	1.297E–04	1.926
$k = 2$	1/20	2.511E–04	–	3.203E–04	–
	1/40	2.741E–05	3.196	4.035E–05	2.989
	1/80	3.317E–06	3.047	5.065E–06	2.994
	1/160	4.112E–07	3.012	6.346E–07	2.997
$k = 3$	1/20	2.574E–05	–	2.508E–05	–
	1/40	2.883E–06	3.158	2.321E–06	3.434
	1/80	3.414E–07	3.078	2.172E–07	3.417
	1/160	4.108E–08	3.055	2.002E–08	3.439
$k = 4$	1/20	9.225E–07	–	1.494E–06	–
	1/40	2.529E–08	5.189	8.022E–08	4.219
	1/80	7.135E–10	5.147	4.164E–09	4.268
	1/160	2.188E–11	5.027	1.990E–10	4.387

1 convergence rates. We also see that Exponential DG is more economical than IMEX DG in the isentropic vortex
 2 example on both uniform and non-uniform meshes. For the Euler systems on the non-uniform mesh, Exponential
 3 DG is comparable to explicit RKDG. Moreover, for the shock problems, EPI2 solutions become 3 times faster than
 4 RK4 solutions when artificial viscosity is employed. This is because the diffusion term becomes a dominant source
 5 to restrict the timestep size of the explicit methods in the shock problems. For all cases, if relaxing the accuracy is
 6 allowed, while time stepsize beyond the maximum stable time stepsize for explicit RKDG is needed, Exponential
 7 DG can be faster than the explicit RKDG.

8 As have been demonstrated, our proposed framework can exploit current and future parallel computing systems
 9 to solve large scale problems. The key explored in the proposed methods do not require a linear solve matrix-
 10 free Krylov-based matrix exponential computations and the DG compact communication stencil. Indeed, we have
 11 numerically shown that Exponential DG methods have favorable strong scaling up to 40K cores and weak scaling
 12 for 16K cores for the Euler isentropic vortex example. Ongoing work is to extend the approach to various partial
 13 differential equations and to scale it beyond hundreds of thousands cores.

14 Declaration of competing interest

15 The authors declare that they have no known competing financial interests or personal relationships that could
 16 have appeared to influence the work reported in this paper.

17 Acknowledgments

18 SK was partially supported by the U.S. Department of Energy, Office of Science, Advanced Scientific Computing
 19 Research Program under contract DE-AC02-06CH11357. The work of TBT was funded in part by DOE grants
 20 DE-SC0010518 and DE-SC0011118, NSF Grant NSF-DMS1620352. We are grateful for the supports.

21 Appendix. Local discontinuous Galerkin methods for viscous Burgers equation

22 We have seen that suboptimal convergence rates for odd orders in Tables 1, 2 and 4. This is related to the use of
 23 central fluxes in the diffusion term. To improve a spatial convergence rate, we employ local discontinuous Galerkin
 24 methods (LDG) [72]. That is, we define the numerical flux u^{**} in (11a) and q^{**} in (12a) by

$$25 \quad u^{**} = \{u\} - [u] \beta, \quad q^{**} = \{q\} + [q] \beta,$$

Table A.14

A shock solution to the viscous Burgers equation with a spatial convergence study using $N_e = \{40, 80, 160\}$ elements is conducted with central (C) flux and local discontinuous Galerkin (LDG) flux for diffusion term. Lax–Friedrich (LF) flux is used for advective term. EXPRB32 scheme with $\Delta t = 5 \times 10^{-5}$ as the time integrator. We take the RK4 solution (with $\Delta t = 5 \times 10^{-7}$, $k = 10$, and $N_e = 160$) as a reference solution to measure the L^2 error at $t = 1$.

	h	LF (C)		LF (LDG)	
		Error	Order	Error	Order
$k = 1$	1/40	1.295E–02	–	1.517E–02	–
	1/80	5.558E–03	1.221	5.960E–03	1.347
	1/160	2.001E–03	1.474	1.838E–03	1.698
$k = 2$	1/40	4.223E–03	–	4.273E–03	–
	1/80	6.722E–04	2.651	7.225E–04	2.564
	1/160	9.852E–05	2.770	1.029E–04	2.812
$k = 3$	1/40	9.976E–04	–	1.159E–03	–
	1/80	1.435E–04	2.797	1.672E–04	2.793
	1/160	1.224E–05	3.551	1.065E–05	3.972
$k = 4$	1/40	3.606E–04	–	4.442E–04	–
	1/80	2.728E–05	3.724	2.256E–05	4.299
	1/160	8.084E–07	5.077	7.304E–07	4.949

where we take $\beta = 0.5$.²¹ Indeed, we numerically observe that the spatial convergence rates increase to $k + 1$ for odd orders in the case with the time-independent smooth solution as shown in Table A.12. We also see that the spatial convergence rates for odd orders are improved up to 0.45 compared with central flux for time-dependent problems in Tables A.13 and A.14. The spatial convergence results are encouraging, thus, we will consider to incorporate LDG methods for developing Navier–Stokes models in the future.

References

- [1] W.H. Reed, T.R. Hill, Triangular Mesh Methods for the Neutron Transport Equation, Tech. Rep. LA-UR-73-479, Los Alamos Scientific Laboratory, 1973.
- [2] P. LeSaint, P.A. Raviart, On a finite element method for solving the neutron transport equation, in: C. de Boor (Ed.), Mathematical Aspects of Finite Element Methods in Partial Differential Equations, Academic Press, 1974, pp. 89–145.
- [3] C. Johnson, J. Pitkäranta, An analysis of the discontinuous Galerkin method for a scalar hyperbolic equation, Math. Comp. 46 (173) (1986) 1–26.
- [4] M.F. Wheeler, An elliptic collocation-finite element method with interior penalties, SIAM J. Numer. Anal. 15 (1) (1978) 152–161.
- [5] D.N. Arnold, An interior penalty finite element method with discontinuous elements, SIAM J. Numer. Anal. 19 (4) (1982) 742–760.
- [6] B. Cockburn, G.E. Karniadakis, C.-W. Shu, The development of discontinuous Galerkin methods, in: Discontinuous Galerkin Methods, Springer, 2000, pp. 3–50.
- [7] D.N. Arnold, F. Brezzi, B. Cockburn, L.D. Marini, Unified analysis of discontinuous Galerkin methods for elliptic problems, SIAM J. Numer. Anal. 39 (5) (2002) 1749–1779.
- [8] R. Liu, Discontinuous Galerkin Finite Element Solution for Poromechanics (Ph.D. thesis), The University of Texas at Austin, 2004.
- [9] R.D. Nair, S.J. Thomas, R.D. Loft, A discontinuous Galerkin global shallow water model, Mon. Weather Rev. 133 (4) (2005) 876–888.
- [10] F.X. Giraldo, T. Warburton, A high-order triangular discontinuous Galerkin oceanic shallow water model, Internat. J. Numer. Methods Fluids 56 (2008) 899–925.
- [11] F.X. Giraldo, M. Restelli, High-order semi-implicit time-integrators for a triangular discontinuous Galerkin oceanic shallow water model, Internat. J. Numer. Methods Fluids 63 (2010) 1077–1102.
- [12] N. Wintermeyer, A.R. Winters, G.J. Gassner, D.A. Kopriva, An entropy stable nodal discontinuous Galerkin method for the two dimensional shallow water equations on unstructured curvilinear meshes with discontinuous bathymetry, J. Comput. Phys. 340 (2017) 200–242.
- [13] F. Bassi, A. Crivellini, S. Rebay, M. Savini, Discontinuous Galerkin solution of the Reynolds-averaged navier–stokes and $k-\omega$ turbulence model equations, Comput. & Fluids 34 (4–5) (2005) 507–540.
- [14] G.J. Gassner, A.R. Winters, D.A. Kopriva, Split form nodal discontinuous Galerkin schemes with summation-by-parts property for the compressible Euler equations, J. Comput. Phys. 327 (2016) 39–66.

²¹ Lax–Friedrich fluxes are used for $(\bar{u}u)^*$ and $\left(\frac{u^2}{2}\right)^*$ in (12b).

- 1 [15] L. Fezoui, S. Lanteri, S. Lohrengel, S. Piperno, Convergence and stability of a discontinuous Galerkin time-domain method for the
2 3D heterogeneous Maxwell equations on unstructured meshes, *ESAIM Math. Model. Numer. Anal.* 39 (6) (2005) 1149–1176.
- 3 [16] T. Bui-Thanh, O. Ghattas, Analysis of an hp-nonconforming discontinuous Galerkin spectral element method for wave propagation,
4 *SIAM J. Numer. Anal.* 50 (3) (2012) 1801–1826.
- 5 [17] L. Noels, R. Radovitzky, An explicit discontinuous Galerkin method for non-linear solid dynamics: Formulation, parallel implementation
6 and scalability properties, *Internat. J. Numer. Methods Engrg.* 74 (9) (2008) 1393–1420.
- 7 [18] S. Tirupathi, J.S. Hesthaven, Y. Liang, Modeling 3D magma dynamics using a discontinuous Galerkin method, *Commun. Comput.*
8 *Phys.* 18 (1) (2015) 230–246.
- 9 [19] L. Demkowicz, *Computing with hp-adaptive Finite Elements: Volume 1 One and Two Dimensional Elliptic and Maxwell Problems*,
10 Chapman and Hall/CRC, 2006.
- 11 [20] A. Kanevsky, M.H. Carpenter, D. Gottlieb, J.S. Hesthaven, Application of implicit–explicit high–order Runge–Kutta methods to
12 discontinuous Galerkin schemes, *J. Comput. Phys.* 225 (2) (2007) 1753–1781.
- 13 [21] U.M. Ascher, S.J. Ruuth, R.J. Spiteri, Implicit-explicit Runge-Kutta methods for time-dependent partial differential equations, *Appl.*
14 *Numer. Math.* 25 (2) (1997) 151–167.
- 15 [22] C.A. Kennedy, M.H. Carpenter, Additive Runge-Kutta schemes for convection-diffusion-reaction equations, *Appl. Numer. Math.* 44
16 (1–2) (2003) 139–181.
- 17 [23] L. Pareschi, G. Russo, Implicit-explicit Runge-Kutta schemes and applications to hyperbolic systems with relaxation, *J. Sci. Comput.*
18 25 (1–2) (2005) 129–155.
- 19 [24] M. Feistauer, V. Dolejsi, V. Kucera, On the discontinuous Galerkin method for the simulation of compressible flow with wide range
20 of Mach numbers, *Comput. Vis. Sci.* 10 (2007) 17–27.
- 21 [25] M. Restelli, F.X. Giraldo, A conservative discontinuous Galerkin semi-implicit formulation for the Navier-Stokes equations in
22 non-hydrostatic mesoscale modeling, *SIAM J. Sci. Comput.* 31 (2009) 2231–2257.
- 23 [26] S. Kang, F.X. Giraldo, T. Bui-Thanh, IMEX HDG-DG: A coupled implicit hybridized discontinuous Galerkin and explicit discontinuous
24 Galerkin approach for shallow water systems, *J. Comput. Phys.* (2019) 109010.
- 25 [27] M. Caliarì, M. Vianello, L. Bergamaschi, Interpolating discrete advection–diffusion propagators at Leja sequences, *J. Comput. Appl.*
26 *Math.* 172 (1) (2004) 79–99.
- 27 [28] E. Celledoni, D. Cohen, B. Owren, Symmetric exponential integrators with an application to the cubic Schrödinger equation, *Found.*
28 *Comput. Math.* 8 (3) (2008) 303–317.
- 29 [29] M.A. Botchev, D. Harutyunyan, J.J. van der Vegt, The Gautschi time stepping scheme for edge finite element discretizations of the
30 Maxwell equations, *J. Comput. Phys.* 216 (2) (2006) 654–686.
- 31 [30] M. Tokman, P. Bellan, Three-dimensional model of the structure and evolution of coronal mass ejections, *Astrophys. J.* 567 (2) (2002)
32 1202.
- 33 [31] S.-J. Li, L.-S. Luo, Z.J. Wang, L. Ju, An exponential time-integrator scheme for steady and unsteady inviscid flows, *J. Comput. Phys.*
34 365 (2018) 206–225.
- 35 [32] G.L. Kooij, M.A. Botchev, B.J. Geurts, An exponential time integrator for the incompressible Navier–Stokes equation, *SIAM J. Sci.*
36 *Comput.* 40 (3) (2018) B684–B705.
- 37 [33] J.C. Schulze, P.J. Schmid, J.L. Sesterhenn, Exponential time integration using Krylov subspaces, *Internat. J. Numer. Methods Fluids*
38 60 (6) (2009) 591–609.
- 39 [34] S.-J. Li, L. Ju, Exponential time-marching method for the unsteady Navier-Stokes equations, in: *AIAA Scitech 2019 Forum*, 2019, pp.
40 0907.
- 41 [35] C. Clancy, J.A. Pudykiewicz, On the use of exponential time integration methods in atmospheric models, *Tellus A* 65 (1) (2013)
42 20898.
- 43 [36] I. Moret, On RD-rational Krylov approximations to the core-functions of exponential integrators, *Numer. Linear Algebra Appl.* 14 (5)
44 (2007) 445–457.
- 45 [37] S. Ragni, Rational Krylov methods in exponential integrators for european option pricing, *Numer. Linear Algebra Appl.* 21 (4) (2014)
46 494–512.
- 47 [38] H. Tal-Ezer, On restart and error estimation for Krylov approximation of $w = f(a)v$, *SIAM J. Sci. Comput.* 29 (6) (2007) 2426–2441.
- 48 [39] M. Afanasjew, M. Eiermann, O.G. Ernst, S. Güttel, Implementation of a restarted Krylov subspace method for the evaluation of matrix
49 functions, *Linear Algebra Appl.* 429 (10) (2008) 2293–2314.
- 50 [40] M.A. Botchev, A block Krylov subspace time-exact solution method for linear ordinary differential equation systems, *Numer. Linear*
51 *Algebra Appl.* 20 (4) (2013) 557–574.
- 52 [41] G.L. Kooij, M.A. Botchev, B.J. Geurts, A block Krylov subspace implementation of the time-parallel Paraexp method and its extension
53 for nonlinear partial differential equations, *J. Comput. Appl. Math.* 316 (2017) 229–246.
- 54 [42] J. Niesen, W.M. Wright, Algorithm 919: A Krylov subspace algorithm for evaluating the ϕ -functions appearing in exponential integrators,
55 *ACM Trans. Math. Softw.* 38 (3) (2012) 22.
- 56 [43] S. Gaudreault, G. Rainwater, M. Tokman, Kiops: A fast adaptive Krylov subspace solver for exponential integrators, *J. Comput. Phys.*
57 372 (2018) 236–255.
- 58 [44] V.T. Luan, J.A. Pudykiewicz, D.R. Reynolds, Further development of efficient and accurate time integration schemes for meteorological
59 models, *J. Comput. Phys.* 376 (2019) 817–837.
- 60 [45] W.E. Arnoldi, The principle of minimized iterations in the solution of the matrix eigenvalue problem, *Quart. Appl. Math.* 9 (1) (1951)
61 17–29.
- 62 [46] A. Koskela, Approximating the matrix exponential of an advection-diffusion operator using the incomplete orthogonalization method,
63 in: *Numerical Mathematics and Advanced Applications-ENUMATH 2013*, Springer, 2015, pp. 345–353.

- [47] H.D. Vo, R.B. Sidje, Approximating the large sparse matrix exponential using incomplete orthogonalization and Krylov subspaces of variable dimension, *Numer. Linear Algebra Appl.* 24 (3) (2017) e2090. 1
- [48] M. Tokman, Efficient integration of large stiff systems of ODEs with exponential propagation iterative (EPI) methods, *J. Comput. Phys.* 213 (2) (2006) 748–776. 2
- [49] D.L. Michels, G.A. Sobottka, A.G. Weber, Exponential integrators for stiff elastodynamic problems, *ACM Trans. Graph.* 33 (1) (2014) 7. 3
- [50] D.L. Michels, V.T. Luan, M. Tokman, A stiffly accurate integrator for elastodynamic problems, *ACM Trans. Graph.* 36 (4) (2017) 116. 4
- [51] F. Giraldo, M. Restelli, High-order semi-implicit time-integrators for a triangular discontinuous Galerkin oceanic shallow water model, *Internat. J. Numer. Methods Fluids* 63 (9) (2010) 1077–1102. 5
- [52] B. Skaflestad, W.M. Wright, The scaling and modified squaring method for matrix functions related to the exponential, *Appl. Numer. Math.* 59 (3–4) (2009) 783–799. 6
- [53] R.A. Horn, R.A. Horn, C.R. Johnson, *Topics in Matrix Analysis*, Cambridge university press, 1994. 7
- [54] R.A. Friesner, L.S. Tuckerman, B.C. Dornblaser, T.V. Russo, A method for exponential propagation of large systems of stiff nonlinear differential equations, *J. Sci. Comput.* 4 (4) (1989) 327–354. 8
- [55] E. Gallopoulos, Y. Saad, Efficient solution of parabolic equations by Krylov approximation methods, *SIAM J. Sci. Stat. Comput.* 13 (5) (1992) 1236–1264. 9
- [56] M. Hochbruck, C. Lubich, H. Selhofer, Exponential integrators for large systems of differential equations, *SIAM J. Sci. Comput.* 19 (5) (1998) 1552–1574. 10
- [57] R.B. Sidje, Expokit: A software package for computing matrix exponentials, *ACM Trans. Math. Softw.* 24 (1) (1998) 130–156. 11
- [58] A.H. Al-Mohy, N.J. Higham, A new scaling and squaring algorithm for the matrix exponential, *SIAM J. Matrix Anal. Appl.* 31 (3) (2009) 970–989. 12
- [59] L.C. Wilcox, G. Stadler, C. Burstedde, O. Ghattas, A high-order discontinuous Galerkin method for wave propagation through coupled elastic–acoustic media, *J. Comput. Phys.* 229 (24) (2010) 9373–9396. 13
- [60] P.L. Roe, Approximate Riemann solvers, parametric vectors, and difference schemes, *J. Comput. Phys.* 43 (2) (1981) 357–372. 14
- [61] K. Masatsuka, *I Do Like CFD*, Vol. 1, Lulu.com, 2013. 15
- [62] J.-L. Guermond, R. Pasquetti, B. Popov, Entropy viscosity method for nonlinear conservation laws, *J. Comput. Phys.* 230 (11) (2011) 4248–4267. 16
- [63] V. Zingan, J.-L. Guermond, J. Morel, B. Popov, Implementation of the entropy viscosity method with the discontinuous Galerkin method, *Comput. Methods Appl. Mech. Engrg.* 253 (2013) 479–490. 17
- [64] G.J. Gassner, A.R. Winters, F.J. Hindenlang, D.A. Kopriva, The BR1 scheme is stable for the compressible Navier–Stokes equations, *J. Sci. Comput.* 77 (1) (2018) 154–200. 18
- [65] I. Babuvska, Error bounds for finite element method, *Numer. Math.* 16 (1971) 322–333. 19
- [66] I. Babuvska, M. Suri, The hp -version of the finite element method with quasiuniform meshes, *Math. Modelling Numer. Anal.* 21 (1987) 199–238. 20
- [67] I. Babuvska, M. Suri, The p and h - p version of the finite element method, basic principles and properties, *SIAM Rev.* 36 (4) (1994) 578–632. 21
- [68] A. Ern, J.-L. Guermond, *Theory and Practice of Finite Elements*, in: *Applied Mathematical Sciences*, vol. 159, Springer-Verlag, 2004. 22
- [69] P.G. Ciarlet, *The Finite Element Method for Elliptic Problems*, in: *Classics in Applied Mathematics*, vol. 40, SIAM (SIAM), Philadelphia, PA, 2002, reprint of the 1978 original [North-Holland, Amsterdam; MR0520174 (58 #25001)]. 23
- [70] K.-J. Engel, R. Nagel, One-parameter semigroups for linear evolution equations, in: *Semigroup Forum*, Vol. 63, Springer, 2001, pp. 278–280. 24
- [71] M. Hochbruck, A. Ostermann, Exponential integrators, *Acta Numer.* 19 (2010) 209–286. 25
- [72] B. Cockburn, C.-W. Shu, The local discontinuous Galerkin method for time-dependent convection-diffusion systems, *SIAM J. Numer. Anal.* 35 (6) (1998) 2440–2463. 26
- [73] Y. Zhou, G. Wei, High resolution conjugate filters for the simulation of flows, *J. Comput. Phys.* 189 (1) (2003) 159–179. 27
- [74] V.T. Luan, Fourth-order two-stage explicit exponential integrators for time-dependent PDEs, *Appl. Numer. Math.* 112 (2017) 91–103. 28
- [75] P.G. Drazin, W.H. Reid, *Hydrodynamic Stability*, Cambridge university press, 2004. 29
- [76] V. Springel, E pur si muove: Galilean-invariant cosmological hydrodynamical simulations on a moving mesh, *Mon. Not. R. Astron. Soc.* 401 (2) (2010) 791–851. 30
- [77] D. Lecoanet, M. McCourt, E. Quataert, K.J. Burns, G.M. Vasil, J.S. Oishi, B.P. Brown, J.M. Stone, R.M. O’Leary, A validated non-linear Kelvin–Helmholtz benchmark for numerical hydrodynamics, *Mon. Not. R. Astron. Soc.* 455 (4) (2016) 4274–4288. 31
- [78] R. Liska, B. Wendroff, Comparison of several difference schemes on 1D and 2D test problems for the Euler equations, *SIAM J. Sci. Comput.* 25 (3) (2003) 995–1017. 32